

Distinct guard cell-specific remodeling of chromatin accessibility during abscisic acid- and CO₂-dependent stomatal regulation

Charles A. Seller^{a,1} and Julian I. Schroeder^{a,1}

Edited by Dominique Bergmann, Stanford University, Stanford, CA; received June 29, 2023; accepted November 7, 2023

In plants, epidermal guard cells integrate and respond to numerous environmental signals to control stomatal pore apertures, thereby regulating gas exchange. Chromatin structure controls transcription factor (TF) access to the genome, but whether large-scale chromatin remodeling occurs in guard cells during stomatal movements, and in response to the hormone abscisic acid (ABA) in general, remains unknown. Here, we isolate guard cell nuclei from Arabidopsis thaliana plants to examine whether the physiological signals, ABA and CO₂ (carbon dioxide), regulate guard cell chromatin during stomatal movements. Our cell type-specific analyses uncover patterns of chromatin accessibility specific to guard cells and define cis-regulatory sequences supporting guard cell-specific gene expression. We find that ABA triggers extensive and dynamic chromatin remodeling in guard cells, roots, and mesophyll cells with clear patterns of cell type specificity. DNA motif analyses uncover binding sites for distinct TFs enriched in ABA-induced and ABA-repressed chromatin. We identify the Abscisic Acid Response Element (ABRE) Binding Factor (ABF) bZIP-type TFs that are required for ABA-triggered chromatin opening in guard cells and roots and implicate the inhibition of a clade of bHLH-type TFs in controlling ABA-repressed chromatin. Moreover, we demonstrate that ABA and CO₂ induce distinct programs of chromatin remodeling, whereby elevated atmospheric CO₂ had only minimal impact on chromatin dynamics. We provide insight into the control of guard cell chromatin dynamics and propose that ABA-induced chromatin remodeling primes the genome for abiotic stress resistance.

chromatin | guard cells | stomata | plant hormones | transcription factors

Organisms evolved mechanisms that connect the activity of their genome to the conditions in their environment. Developmental and environmental signals can impact the genome by regulating transcription factor (TF) binding to cognate DNA sequences known as cis-regulatory elements (CRE) (1). In eukaryotes, this regulation occurs in the context of chromatin where nucleosomes can impede TF binding to target sequences (2, 3). Consequently, the remodeling of chromatin structure to allow access of TFs to target DNA is thought to be a key step in gene regulation. Plant hormones are key signaling molecules controlling numerous aspects of plant life that coordinate genome activity with environmental conditions (4, 5). Recent studies have provided insight into how chromatin structure changes during plant development (6-12) and in response to environmental and hormonal stimuli (13-15).

Here, we focus on the abscisic acid (ABA) signal transduction pathway to explore the connection between hormone signaling and chromatin structure in plants. ABA is a major plant stress hormone that accumulates in cells and tissues experiencing abiotic stress, especially those linked to plant water status (16–18). ABA signals through a well-understood core module consisting of PYR/PYL/RCAR ABA receptor proteins, PP2C protein phosphatases, and SnRK2 protein kinases (19-21). Upon ABA binding, PYR/PYL/RCAR receptor proteins inactivate PP2C phosphatases resulting in the derepression of SnRK2 kinases. ABA-activated SnRK2 kinases then phosphorylate and thereby directly regulate downstream proteins including numerous TFs (22–28). Consequently, ABA triggers the differential expression of thousands of genes in the Arabidopsis thaliana genome (4, 29–31). However, it remains unclear, especially at the genome scale, whether ABA signaling reshapes chromatin structure and how ABA-regulated TFs might function in the context

One well-known action of ABA is to trigger the closure of the stomatal aperture (17). Stomata are small pores on the surface of the leaf that mediate gas exchange and are formed by a pair of specialized epidermal cells known as guard cells. Guard cells perceive and respond to multiple environmental and hormonal cues in order to optimally regulate the size of the stomatal pore (32–34). For instance, some signals such as elevated atmospheric

Significance

Specialized leaf cells called guard cells integrate environmental cues to optimally control the size of microscopic stomatal pores. The hormone abscisic acid (ABA), a key regulator of plant drought responses, and changes in atmospheric CO₂ (carbon dioxide) concentration are signals that control stomatal aperture size, but whether these signals also regulate genome packaging into chromatin is unknown. Using guard cell-specific chromatin profiling, we uncovered regulatory DNA sequences driving specific gene expression in this cell type. We also found that ABA triggers extensive and persistent changes to chromatin structure in guard cells. Unexpectedly, exposure of plants to elevated atmospheric CO₂ had only minimal impact on chromatin dynamics. Furthermore, we identified the specific transcription factors that regulate ABA-induced chromatin dynamics in guard cells.

Author affiliations: aSchool of Biological Sciences, Cell and Developmental Biology Department, University of California San Diego, La Jolla, CA 92093-0116

Author contributions: C.A.S. and J.I.S. designed research; C.A.S. performed research; C.A.S. contributed new reagents/analytic tools; C.A.S. analyzed data; and C.A.S. and J.I.S. wrote the paper.

The authors declare no competing interest.

This article is a PNAS Direct Submission.

Copyright © 2023 the Author(s). Published by PNAS. This article is distributed under Creative Commons Attribution-NonCommercial-NoDerivatives License 4.0

¹To whom correspondence may be addressed. Email: cseller@ucsd.edu or jischroeder@ucsd.edu.

This article contains supporting information online at https://www.pnas.org/lookup/suppl/doi:10.1073/pnas. 2310670120/-/DCSupplemental.

Published December 19, 2023.

carbon dioxide (CO₂), ABA, and the immune elicitor Flg22 trigger stomatal closure, while reduced CO2, light, and heat trigger stomatal opening. Because of their exquisite environmental reactivity, guard cells are an excellent model cell system to investigate how different physiological signals regulate chromatin structure in a cell type-specific manner. Although the recent application of single-cell RNA-seq to Arabidopsis has expanded our understanding of gene regulation, these studies often focus on plate-grown seedlings (35, 36) and/or resulted in datasets with limited representation of guard cells (37, 38). To apply epigenomic techniques to the question of how guard cells respond to different stimuli, new protocols are needed that can isolate large numbers of pure guard cells from soil-grown plants, a more relevant setting for physiological studies.

In this paper, we describe the development of an approach to purify guard cell nuclei and by deploying this method uncover how guard cell chromatin structure changes in response to different stimuli that drive stomatal movements. We profiled the chromatin and transcriptional reprogramming in response to ABA in three different developmental contexts-roots, mesophyll cells, and guard cells. We map thousands of loci that gain or lose chromatin accessibility in response to ABA and link these regions to coregulated transcripts, uncovering a critical role for chromatin dynamics in controlling ABA-dependent transcription. Furthermore, we show that genome-wide and persistent changes to chromatin structure accompany ABA-induced stomatal closure and that four related basic leucine zipper (bZIP) TFs known as ABRE Binding Factors (ABFs) are required for initiating the majority of ABAinduced chromatin opening. In contrast, we implicate a family of related basic helix-loop-helix (bHLH)-type TFs known as ABA-Kinase Substrates (AKSs) in the maintenance of open chromatin upstream of ABA-repressed genes. Finally, we show that in guard cells, changes to atmospheric CO2 concentration trigger distinct and more limited chromatin remodeling and gene regulatory programs from those mediated by ABA.

Results

ABA Induces Rapid and Genome-Wide Chromatin Remodeling in Roots. As an initial test of the relationship between ABA and chromatin, we focused on A. thaliana seedlings. To measure changes to chromatin structure, we combined fluorescenceactivated nuclei sorting (FANS) with the Assay for Transposase-Accessible Chromatin with sequencing (ATAC-seq), a quantitative measurement of chromatin accessibility across the genome (39, 40). 50,000 nuclei per sample were isolated using FANS (SI Appendix, Fig. S1A). We called 25,753 ATAC-seq peaks across all whole seedling and seedling root libraries (Datasets S1 and S2). Genomic regions coinciding with these peaks are known as Accessible Chromatin Regions (ACRs) and predominantly aligned with upstream regulatory regions in the genome (SI Appendix, Fig. S1 B-E). In contrast, ATAC-seq reads derived from purified genomic DNA did not cluster into defined peaks (SI Appendix, Fig. S1 B and C). We next treated whole seedlings with ABA and profiled chromatin accessibility after 4 h. Differential analysis revealed hundreds of regions that significantly gain and lose accessibility in response to ABA (Fig. 1A and Dataset S3).

To capture the dynamics of ABA-induced chromatin remodeling, we focused on roots which can rapidly take up ABA from their surroundings (41, 42). Using FANS, we isolated root nuclei at three different time points following ABA treatment (after 45, 120, and 240 min) and performed ATAC-seq. Differential analysis revealed that ABA triggers time-dependent changes in chromatin accessibility in roots (Dataset S3). Heatmaps centered over these ABA-regulated ACRs illustrate the progressive impact of ABA on chromatin structure, with more regions of the genome changing in ATAC-signal over time (Fig. 1 B and C). We observed significant changes to chromatin after only 45 min of ABA treatment, with 163 ACRs located in upstream regulatory regions gaining accessibility and 64 losing accessibility (Fig. 1 C and E). After 4 h, ABA had activated 1,293 ACRs and repressed 1,119 ACRs (Fig. 1C and Dataset S3). Interestingly,

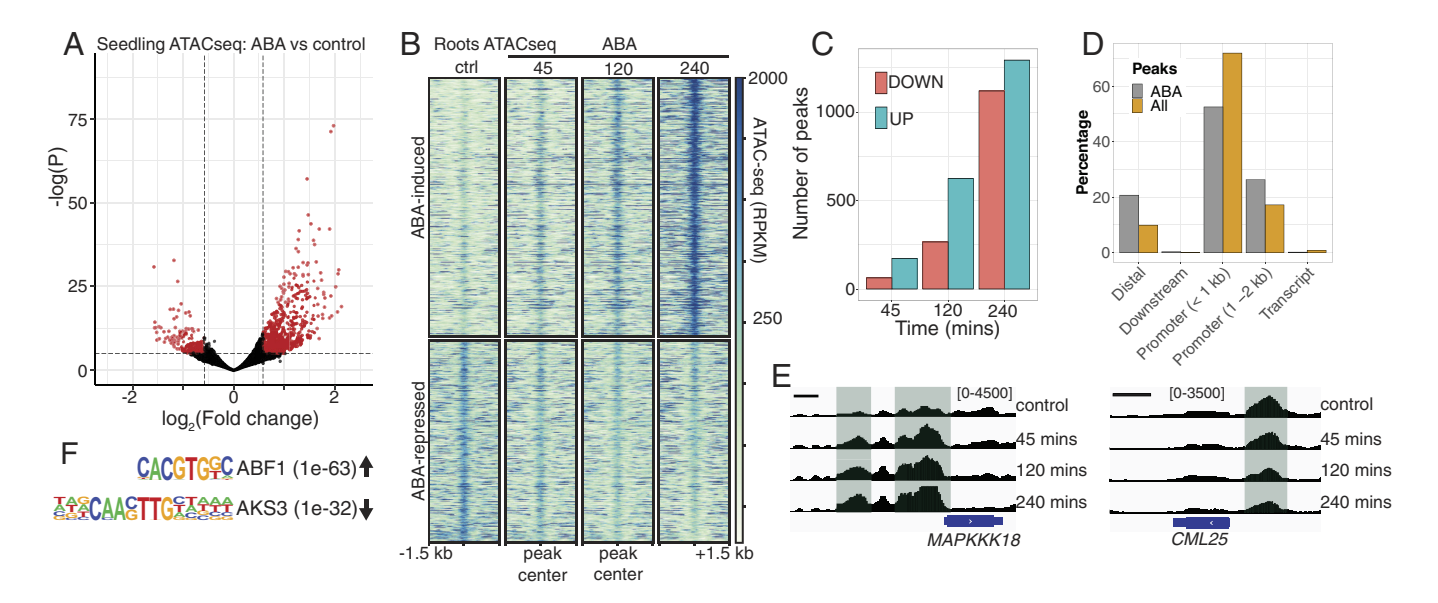


Fig. 1. ABA induces rapid and genome-wide chromatin remodeling in seedlings. (4) Volcano plot of differential ATAC-seq analysis showing regions that significantly change in chromatin accessibility in seedlings after 4 h of ABA treatment. ABA increased accessibility at 666 regions and decreased accessibility at 214 regions (FDR < 0.001 and FC > 1.5, differential peaks colored in red). (B) Heatmap of root nuclei ATAC-seq signal (Reads Per Kilobase per Million or RPKM-normalized) centered over ATAC-seq peaks (±1.5 kb) with ABA-regulated chromatin accessibility during the indicated ABA treatment time course. Across all time points (in min), ABA increased accessibility at 1,293 regions and decreased accessibility at 1,119 regions (FDR < 0.001 and FC > 1.5). (C) Number of ABA-regulated ATAC-seq peaks over time in roots. ABA-induced peaks are colored in blue while ABA-repressed peaks are colored in pink. (D) Distribution among annotated genomic features of either all ATAC-seq peaks (orange) or ABA-regulated ATAC-seq peaks (gray). (E) Genome browser snapshots at two representative genes (MAPKKK18 and CML25) showing changes in ATAC-seq signal in upstream regions following ABA treatment. (Scale bars indicate 500 bp), and gray-green shaded boxes indicate approximate regions of differential accessibility. (P) The TF binding motifs with the highest enrichment (by binomial P-value) in ABA-induced and ABA-repressed chromatin regions in roots.

we found that ABA-regulated ACRs tend to be located further away from transcription start sites (TSS) (>1 kb) than static regions (Fig. 1D). ABA-induced ACRs were most associated with downstream genes enriched for gene ontology (GO) terms such as "response to water deprivation," "response to osmotic stress," and "response to ABA" (Dataset S6).

To explore the role of specific TFs in orchestrating these changes, we performed DNA motif analysis using a set of motifs empirically generated by the in vitro DNA binding assay DAP-seq (43). We found that motifs recognized by ABF/AREB TFs such as ABF1/2/3/4 and ABI5 were highly enriched in ABA-induced ACRs (Fig. 1F, example ABF1, P = 1e-63, Dataset S7). In contrast, we found that ABA-repressed ACRs showed enrichment for motifs recognized by the related bHLH type TFs AKS1, AKS3, and bHLH80 (Fig. 1*F*, example AKS3, *P* = 1e-32, Dataset S7). Notably, both ABF1/2/3/4 and AKS1/2/3 proteins are direct targets of ABA-regulated SnRK2 kinases (22, 24). Previous research has shown a role for ABA-dependent inhibition of bHLH-type AKS TFs in the transcriptional repression of the guard cell K⁺ channel

KAT1 (24, 44). Interestingly, our findings suggest a larger role for the AKS clade of closely related bHLH proteins in the regulation of ABA-repressed genes. We conclude that ABA can trigger rapid and genome-wide chromatin remodeling in root tissue.

Revealing Guard Cell-Specific Patterns of Chromatin Accessibility. Encouraged by our findings in whole seedlings and roots, we next decided to investigate the effect of ABA on chromatin in mature guard cells. We first developed a fluorescence-activated cell sorting (FACS)-based strategy to purify guard cell nuclei from soil-grown plants. Nuclei were labeled by expressing the histone H2B fused to Green Fluorescent Protein (GFP) under the control of the guard cell pGC1 promoter (45). We first confirmed the guard cell specificity of the H2B-GFP fusion in our transgenic lines using fluorescence microscopy (Fig. 2A) and confirmed that ABA treatment did not alter this guard cell-specific expression (SI Appendix, Fig. S2A). We first isolated nuclei from leaf epidermal samples harvested from pGC1:H2B-GFP plants. DAPI-stained nuclei preparations were then analyzed

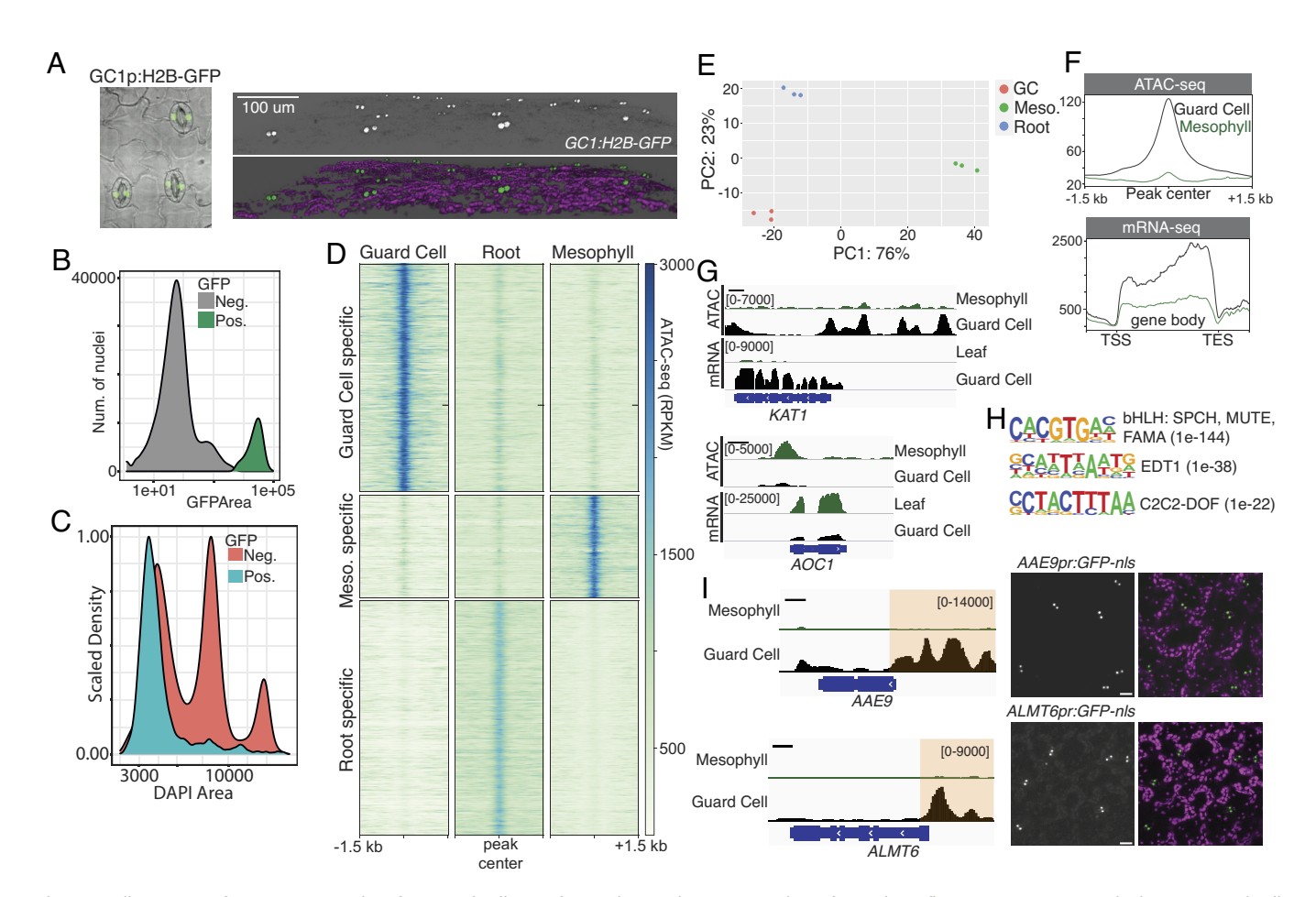


Fig. 2. Cell type-specific epigenomics identifies guard cell-specific regulatory elements. (A) The Left panel is a fluorescence micrograph showing guard cellspecific expression of H2B-GFP. The Right panel shows a 3D reconstruction from confocal imaging of a 5-wk-old GC1p:H2B-GFP leaf (the merged image shows GFP fluorescence in green and chlorophyll fluorescence in magenta). (B) FACS analysis of nuclei (DAPI positive) from GC1p:H2b-GFP plants. A GFP density plot defines two distinct populations separated by GFP intensity. (C) DAPI density plot shows that GFP-positive nuclei (blue population) are primarily diploid, while GFP-negative nuclei (pink population) are distributed over multiple ploidies. (D) Chromatin accessibility heatmaps comparing ATAC-seq signal (RPKM-normalized) in guard cell, mesophyll, or root cell nuclei. ATAC-seq peaks are separated into guard cell-enriched (3,272 ACRs), mesophyll-enriched (1,472 ACRs), and rootenriched (3,364 ACRs) sets defined by differential accessibility (p.adj < 0.001, Fold-Change > 2). (E) Principal component analysis (PCA) comparing ATAC-seq biological replicates derived from guard cell, mesophyll, or root nuclei. (F) A peak-centered ATAC-seq metaplot and a gene body-centered RNA-seq metaplot showing average chromatin accessibility at guard cell-specific peaks and average transcript levels of nearest downstream genes (ATAC-seq peak within -2.5 kb and +0.5 kb of transcription start site). Guard cell-derived signal is shown in black while mesophyll/leaf signal is shown in green. (G) Genome browser images displaying ATAC-seq and RNA-seq signal for the indicated tracks near the guard cell expressed gene KAT1 and the mesophyll cell expressed gene AOC1. (Scale bars indicate 500 bp.) (H) Results of de novo motif analysis are shown along with the best matching known TFs and the enrichment P-values. (I) Transcriptional reporter lines were generated using cloned guard cell-specific ACRs upstream of the genes AAE9 and ALMT6, the positions of the cloned sequences are indicated with orange highlighting on the genome browser images (scale bars indicate 500 bp). Confocal images of reporter expression show GFP fluorescence (Left) or merged GFP (green) and chlorophyll (magenta) fluorescence (Right). (Scale bar represents 20 μm.)

using FACS (SI Appendix, Fig S2B). We could define a clearly separated GFP-positive population among all detected nuclei (Fig. 2B and SI Appendix, Fig. S2C). In contrast to many other cell types in the Arabidopsis leaf, guard cells are diploid, and GFPpositive nuclei from pGC1:H2B-GFP expressing plants had a 2n DNA content while GFP-negative nuclei were distributed among higher ploidy levels (Fig. 2C). Approximately 5% of GFP-positive particles (41 out of 5,037 total from a single FACS run) had DAPI content greater than 2N; however, we sorted only 2N nuclei for downstream applications. This method allowed us to obtain ~30,000 guard cell nuclei with an estimated purity of 98% (SI Appendix, Fig. S2D) from the leaves of 40 to 50 plants. To assay guard cell chromatin structure, nuclei isolated using this method were used to generate ATAC-seq libraries. The resulting libraries were of high quality with clear concentration of peaks in annotated upstream regulatory regions, enrichment of open chromatin fragments (<100 bp) immediately upstream of TSS, strong correlation between biological replicates (SI Appendix, Fig. S2 *E*–*G*), and high FRiP (fraction of reads in peaks) scores (Dataset S1).

In parallel, we generated ATAC-seq samples from root nuclei and from FANS-isolated mesophyll nuclei labeled by expression of H2B-GFP from the promoter of the mesophyll expressed Rubisco small subunit 2B (RBC) gene (SI Appendix, Fig. S3 A-C) (6). For each tissue/cell type, we compared ATAC-seq libraries derived from three biological replicates. We identified 30,985 ATAC-seq peaks across all samples (Dataset S2) and called cell type-enriched peaks using pairwise differential accessibility analysis. Although most ATAC-seq peaks did not differ significantly among cell types, we found 3,272 guard cellenriched ACRs, 1,472 mesophyll-enriched ACRs, and 3,364 root-enriched ACRs (Dataset S2). Heatmaps centered over these regions highlight characteristics of cell/tissue specificity in the observed patterns of chromatin accessibility (Fig. 2D and SI Appendix, Fig. S4A). Importantly, biological replicates derived from the same tissue/cell type clustered together in principal component analysis (PCA) underscoring the robustness of this approach (Fig. 2E).

To evaluate the relationship between guard cell-enriched chromatin accessibility and gene expression, we performed RNA-seq on both whole leaves and guard cell-enriched samples. We found that regions with high chromatin accessibility specifically in guard cells were associated with elevated transcript levels from the adjacent downstream genes, indicating that we are identifying functional CREs (Fig. 2F). Although the correlation between overall promoter chromatin accessibility and downstream transcript level was weak in guard cells (Pearson's r = 0.19, *SI Appendix*, Fig. S4*B*), we found that differentially accessible ACRs showed higher correlation with downstream gene differential expression (Pearson's r = 0.55, *SI Appendix*, Fig. S4C). Examination of individual gene loci like the guard cell expressed gene KAT1 (46-48) illustrated the connection between increased upstream accessibility and increased transcript levels (Fig. 2G and SI Appendix, Fig S4D). By contrast, the mesophyll-expressed gene AOCI had high chromatin accessibility in mesophyll cells, but minimal upstream ATAC-seq signal in guard cells (Fig. 2G). TF binding motif analysis on guard cell-enriched ACRs returned de novo motifs with strong similarity to motifs recognized by known stomatal lineage transcriptional regulators such as the bHLH proteins SPCH, MUTE, and FAMA as well as EDT1 and DOF-type TFs (49-53) (Fig. 2H and Dataset S7). In contrast, we find that WRKY-type TF binding motifs are enriched in regions that are significantly less accessible in guard cells compared to roots and mesophyll cells (Dataset S7). However, these motifs are recognized by large TF families

containing many TFs that are not specific to guard cells, for instance, SPCH and MUTE are active only early during stomatal lineage development (49, 50). By connecting guard cell-specific ACRs with downstream guard cell-enriched transcripts, we were able to define a set of 827 putative regulatory elements preferentially active in guard cells (Dataset S4). To further confirm that our approach identified functional cis-regulatory regions, we generated transcriptional reporter constructs expressing nuclearlocalized GFP under the control of the guard cell-specific ACRs upstream of the malate-transporter encoding gene ALMT6 (54) and the wax biosynthesis enzyme-encoding gene AAE9 (55). Both reporter constructs produced guard cell-specific GFP signal in transgenic Arabidopsis leaves (Fig. 21). In summary, we have developed a robust protocol for isolating pure populations of guard cell nuclei allowing us to find cis-regulatory regions that are active in mature guard cells.

ABA Induces Persistent Chromatin Remodeling in Guard Cells during Stomatal Closure. We next asked whether epigenomic reprogramming occurs during ABA-induced stomatal closure. Soil-grown 6-wk-old plants were sprayed with 50 μM ABA or control solution. After 3 h, we confirmed a stomatal response by infrared photography (Fig. 3A). To determine whether our ABA treatment led to significant transcriptional changes, we performed RNA sequencing on both whole leaf samples (SI Appendix, Fig. S5A) and guard cell-enriched samples (Fig. 3B). We observed that ABA triggered the differential expression of thousands of transcripts in both whole leaves and guard cells (2,142 up-regulated and 1,574 down-regulated in guard cells). As expected, ABA-induced genes are enriched for the pathways response to water deprivation (P-value = 1.7e-22), response to ABA (P-value = 4.47e-18), and "response to salt stress" (SI Appendix, Fig. S5D). Although most of the transcriptional changes induced by ABA were shared between guard cells and whole leaves, we found that 22.7% (488) of ABA-induced transcripts and 42.7% (673) of ABA-repressed transcripts were specific to guard cells (SI Appendix, Fig. S5C and Dataset S5). For instance, ABA-regulated expression of the major facilitator protein-encoding gene AT2G37900 and the gene AAE9 was only evident in guard cells (SI Appendix, Fig. S5*E*).

To evaluate whether ABA changed chromatin accessibility and whether these changes are sustained over time following a single treatment, we isolated guard cell nuclei at 4 h and 24 h after spraying (Fig. 3A). We generated ATAC-seq libraries from three biological replicates per time point. PCA analysis showed that samples clustered together according to treatment (SI Appendix, Fig. S6A). Differential chromatin accessibility analysis found that ABA extensively reshapes chromatin structure in guard cells with 2,323 ACRs gaining accessibility and 1,657 ACRs losing accessibility across the treatment time course (Fig. 3C, SI Appendix, Fig. S7 A and B, and Dataset S3). We next analyzed the temporal characteristics of this response by comparing the ATAC-seq datasets from the 4-h and 24-h time points. Our results allowed us to define three categories of ABA-regulated ACRs—early, sustained, and late (Fig. 3D). Strikingly, we found that 1,093 of the 2,079 (52.6%) ACRs opened by ABA at 4 h remained open after 24 h. Of the 975 ACRs closed by ABA at 4 h 594 (61%) remained closed at 24 h. Additionally, we found 230 ACRs gained and 682 ACRs lost accessibility only 24 h after ABA treatment (Fig. 3D). Interestingly, we found differences in downstream gene GO term enrichment between early and late ACRs. For example, the terms "response to light" and "defense response" were strongly enriched in ABA-repressed ACRs only at 24 h after ABA treatment (Dataset S6).

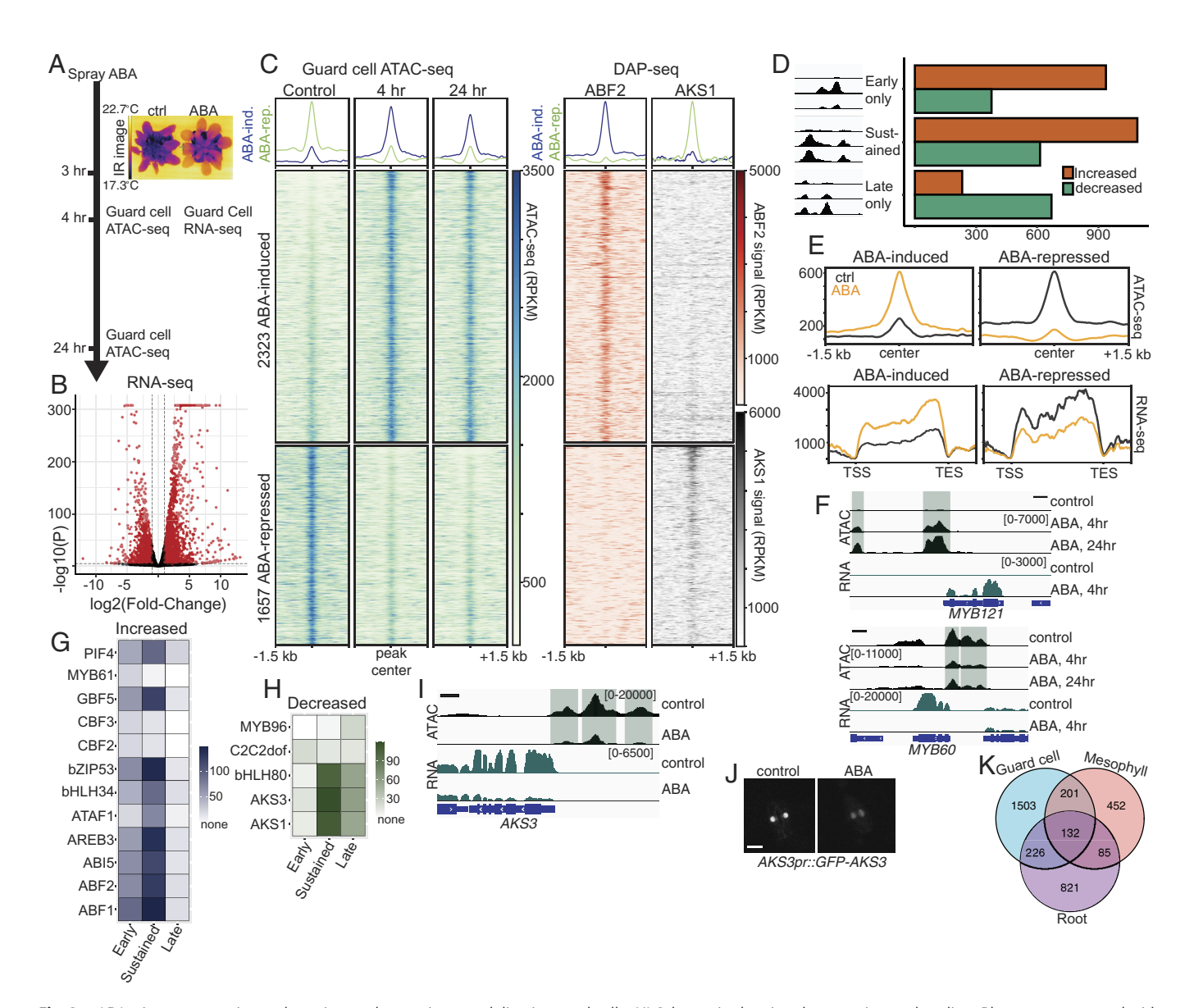


Fig. 3. ABA triggers extensive and persistent chromatin remodeling in guard cells. (A) Schematic showing the experimental outline. Plants were sprayed with ABA, and infrared images were taken using a thermal camera to assess stomatal closure. Guard cell nuclei were purified at 4 h and 24 h after treatment and used for ATAC-seq. (B) Volcano plot of guard cell-enriched RNA-seq data showing that ABA up-regulates 2,142 transcripts and down-regulates 1,574 transcripts (FDR < 0.001, FC > 2.0). Differentially expressed transcripts are colored in red. (C) Heatmaps and profile plots of ATAC-seq signal (RPKM-normalized) in guard cell nuclei centered (±1.5 kb) over 2,323 regions with ABA-induced chromatin accessibility and 1,657 regions with ABA-repressed chromatin accessibility (FDR < 0.001, FC > 2.0). The adjacent heatmaps show DAP-seq signal for ABF2 (in red) and AKS1 (in black) centered over the same ABA-regulated ACRs, data from refs. 39 and 56. (D) Comparison of ABA-regulated peaks from 4-h and 24-h time points separated ACRs into three categories—early only, sustained (both early and late), and late only. The bar graph shows the number of ABA-increased and -decreased regions in each category. (E, Top) Metaplots showing average ATAC-seq signal centered over either ABA-induced or ABA-repressed ACRs and (Bottom) RNA-seq metaplots showing average transcript level centered over gene bodies downstream of the same ACRs. Signal from ABA-treated plants is shown in orange, and signal from control-treated plants is shown in black. (F) Genome browser images showing guard cell ATAC-seq and RNA-seq signal at a representative ABA-induced gene (MYB121) and an ABA-repressed gene (MYB60). (Scale bars indicated 500 bp.) (G and H) Heatmaps showing TF binding motif enrichments [-log(P-value)] in ABA-increased (G) and ABA-decreased (H) ATAC-seq peaks. (I) Genome browser images showing guard cell ATAC-seq and RNA-seq signal at the AKS3 gene. (Scale bars indicated 500 bp.) (J) Fluorescence micrograph showing expression of AKS3pr::GFP-AKS3 in guard cells after treatment with control or ABA (4 h). (k) Overlap of ABA-induced accessible regions in guard cell nuclei, mesophyll nuclei, and root nuclei.

Consistent with our observations in seedling roots (Fig. 1D), we found that ABA-regulated ATAC-seq peaks in guard cells reside further away from TSS than nonregulated peaks (>1 kb), indicating that distal regulation may be a characteristic of ABA-controlled CREs (SI Appendix, Fig. S6B). ABA-induced ACRs in guard cells are clearly associated with downstream genes that are up-regulated transcriptionally by ABA, while ABA-repressed ACRs are associated with genes down-regulated by ABA (Fig. 3E). Indeed, ABA-induced changes in chromatin accessibility were correlated with ABA-induced differential expression of downstream genes (r = 52, SI Appendix, Fig. S6C). Examination of individual genes like the ABA-up-regulated MYB121 and the ABA-down-regulated MYB60 (56) illustrate the connection between upstream chromatin accessibility and transcript levels (Fig. 3F). Interestingly, we found that ABA modifies chromatin accessibility upstream of many known regulators of stomatal conductance including *KAT1*, NCED3, and HT1 (57) as well as many other genes with no known stomatal functions (SI Appendix, Fig. S6 D-K and Dataset S3).

We next performed TF binding motif analysis on early, sustained, and late ABA-regulated ACRs using a set of DAP-seq derived motifs (43) restricted to those TFs with guard cell expression in our RNA-seq datasets. Both early and sustained ABA-induced ACRs had strong enrichment for motifs recognized by ABRE-binding TFs including ABI5, ABF1,2, and 3 (Fig. 3*G*). Interestingly, we found that the motifs recognized by CBF2, CBF3, and MYB61 (58–60) were preferentially enriched in early ABA-induced ACRs. ABA-repressed ACRs showed strong enrichment for motifs recognized by a clade of related bHLH-type TFs (SI Appendix, Fig. S6L) including AKS1, AKS3, and bHLH80 in both sustained and late categories (Fig. 3*H*). In contrast, MYB96 motifs were enriched only in late-appearing ABA-repressed ACRs (Fig. 3H). Collectively, our results demonstrate that ABA can induce persistent changes to chromatin in guard cells and expose the temporal regulation of different TFs during this response.

By analyzing published genome-wide DAP-seq datasets (39, 56), we found strong ABF2 DAP-seq signal coincident with ABA-induced ACRs in guard cells (Fig. 3C). DAP-seq signals for ABF1, ABF3, and ABF4 were also enriched over regions that gain accessibility in response to ABA, although to a lesser extent than ABF2 (SI Appendix, Fig. S6M). In contrast, ABA-repressed ACRs contained AKS1 DAP-seq binding sites (Fig. 3C). Additionally, unbiased de novo motif discovery (61) returned motifs similar to ABF1 and AKS3 binding sites as the most enriched in ABA-activated and ABA-repressed ACRs, respectively (P = 1e-119 and P = 1e-57). Metaplots of ATAC-seq signal centered over peaks containing these motifs further supported our observation that ABA elevates chromatin accessibility at ABF binding sites and represses chromatin accessibility at AKS binding sites (SI Appendix, Fig. S6N). Interestingly, ABA closed chromatin upstream of AKS3 and decreased AKS3 transcript levels in guard cells (Fig. 31). We also observed that GFP-AKS3 signal decreased in ABA-treated guard cells when expressed from its native promoter (Fig. 3/).

Furthermore, by comparing ABA-induced ACRs from guard cells, mesophyll cells (SI Appendix, Fig. S3 E-G), and root cells (Fig. 1), we uncovered significant tissue/cell type specificity in this response (Fig. 3K and SI Appendix, Fig S7 C-L). Interestingly, we found that ABA had a much larger impact on chromatin accessibility in guard cells than in the other cell types with more ABA-regulated regions (2,079 ACRs compared with 1,293 in roots and 926 in mesophyll) and larger fold changes in accessibility (Dataset S3). In conclusion, we show that ABA drives large-scale changes to chromatin structure in guard cells and implicate major roles for the activation of ABFs and inhibition of AKSs in this response.

ABF TFs Are Required for ABA-Induced Chromatin Opening in **Guard Cells.** The mechanisms that cause ABA-specific chromatin opening are unknown. Given the strong enrichment of ABF binding motifs in ABA-activated ACRs, and their coincidence with ABF in vitro binding sites, we wondered whether these TFs might be required for reshaping chromatin during ABA-induced stomatal closure. To test this, we used the abf1/2/3/4 (abfx4) quadruple mutant which lacks four related ABF proteins that are prominent during vegetative growth (25, 26). We first performed RNA-seq following ABA treatment on leaves from 6-wk-old abf1/2/3/4 (abfx4) mutant plants (SI Appendix, Fig. S8A). Of the 2,257 transcripts that are up-regulated by ABA in wild-type leaves, 1,897 (~84%) depend on ABF1/2/3/4 (SI Appendix, Fig. S8B). Interestingly, although ABA increased ABF1/2/3/4 transcript levels in guard cells, we did not find that ABA altered chromatin accessibility in the upstream regions near the corresponding genes (SI Appendix, Fig. S8C). We conclude that ABF1/2/3/4 are required for the bulk of ABA-induced gene expression in mature leaf tissue. Plants lacking ABF1/2/3/4 (abfx4) are highly sensitive to drought stress and lose water faster than wild-type plants

in detached leaf assays (26). Consistent with this, we observed that abfx4 mutant plants exhibited higher steady-state stomatal conductances than *Col-0* control plants (*SI Appendix*, Fig. S8*D*).

Under nonstressed conditions, guard cells have a higher ABA concentration than other leaf cell types (42, 62). Recent studies have provided evidence for basal ABA signaling in guard cells and defined important roles for basal ABA in stomatal function (63, 64). By generating guard cell FANS lines in an abfx4 mutant background (SI Appendix, Fig. S9A), we were able to assess the impact of the loss of ABF1/2/3/4 on guard cell chromatin in nonstressed plants. In the absence of ABA treatment, we observed minimal differences in genome-wide patterns of chromatin accessibility between WT and abfx4 guard cells (SI Appendix, Fig S9 and Dataset S3) suggesting that basal ABA signaling in guard cells may regulate mainly posttranscriptional stomatal closing mechanisms but does not significantly regulate chromatin structure.

Next, we asked whether the ABF1/2/3/4 are required for the ability of ABA to reshape chromatin structure. Strikingly, loss of abf1/2/3/4 strongly impaired ABA-induced chromatin opening in guard cells but had less impact on ABA-triggered chromatin closing (Fig. 4A and Dataset S7). Of the 2,079 ABA-induced ACRs, 1,539 (~74%) required ABF1/2/3/4 for gained accessibility (Fig. 4B). ABF-dependent ABA-induced ACRs were strongly enriched for ABREs (example ABF1, P = 1e-86), while ABF-independent ABA-induced ACRs were most strongly enriched for CBF1/2/3 motifs (example CBF1, P = 1e-16) (Dataset S7). Examination of individual loci like the ABA-activated genes DTX37 and HSFA6B revealed a close connection between ABF-dependent increases in upstream chromatin accessibility and ABF-dependent transcription (Fig. 4*C*).

We next performed TF motif analysis on ABA-regulated ACRs in both WT and abfx4 mutant guard cells. As expected, abfx4 mutants were depleted for ABRE motif enrichment in ABA-induced ACRs but notably retained enrichment for AKS1, AKS3, and bHLH80 motifs in ABA-repressed ACRs (Fig. 4D and Dataset S7). Additionally, although most TF binding sites lost enrichment in ABA-induced ACRs in the absence of ABF1/2/3/4, we found that enrichment for motifs bound by CBF1/2/3 was preserved. TF binding motifs are often information poor and the presence of a motif at a genomic location does not always lead to TF action. Analysis of published ABF1/2/3/4 binding assays conducted on naked genomic DNA (65) uncovered 11,334 binding sites, but only 1,315 resided within ABA-induced ACRs in guard cells (Fig. 4E). However, ABA-induced chromatin opening at these ACRs containing ABF-binding sites was strongly impaired in abfx4 mutant guard cells (Fig. 4F). We reasoned that chromatin structure may determine which in vitro ABF binding sites are functional. To test this idea, we examined whether ABF DAP-seq peaks found within ABAinduced ACRs could predict ABA-activated transcription. Using our guard cell RNA-seq data, we found that ABF binding sites that reside within regions of ABA-regulated open chromatin were more strongly associated with downstream ABA-induced transcripts than were an equal number of random ABF-binding sites (Fig. 4G).

To examine the temporal characteristics of ABF-dependent chromatin remodeling, we focused on roots where ABA can reshape chromatin by 45 min (Fig. 1C). We performed ATAC-seq on isolated *abfx4* mutant root nuclei over an ABA treatment time course and found that ABA fails to drive progressive chromatin opening in this background (SI Appendix, Fig. S10). In abfx4 mutant roots, 45 min of ABA treatment induced only 2 ACRs compared to 163 in wild-type roots (Fig. 4H). By 2 h of ABA treatment, only 27 ABA-induced ACRs were present in abfx4 mutants compared with 601 in wild type (Fig. 4H, SI Appendix,

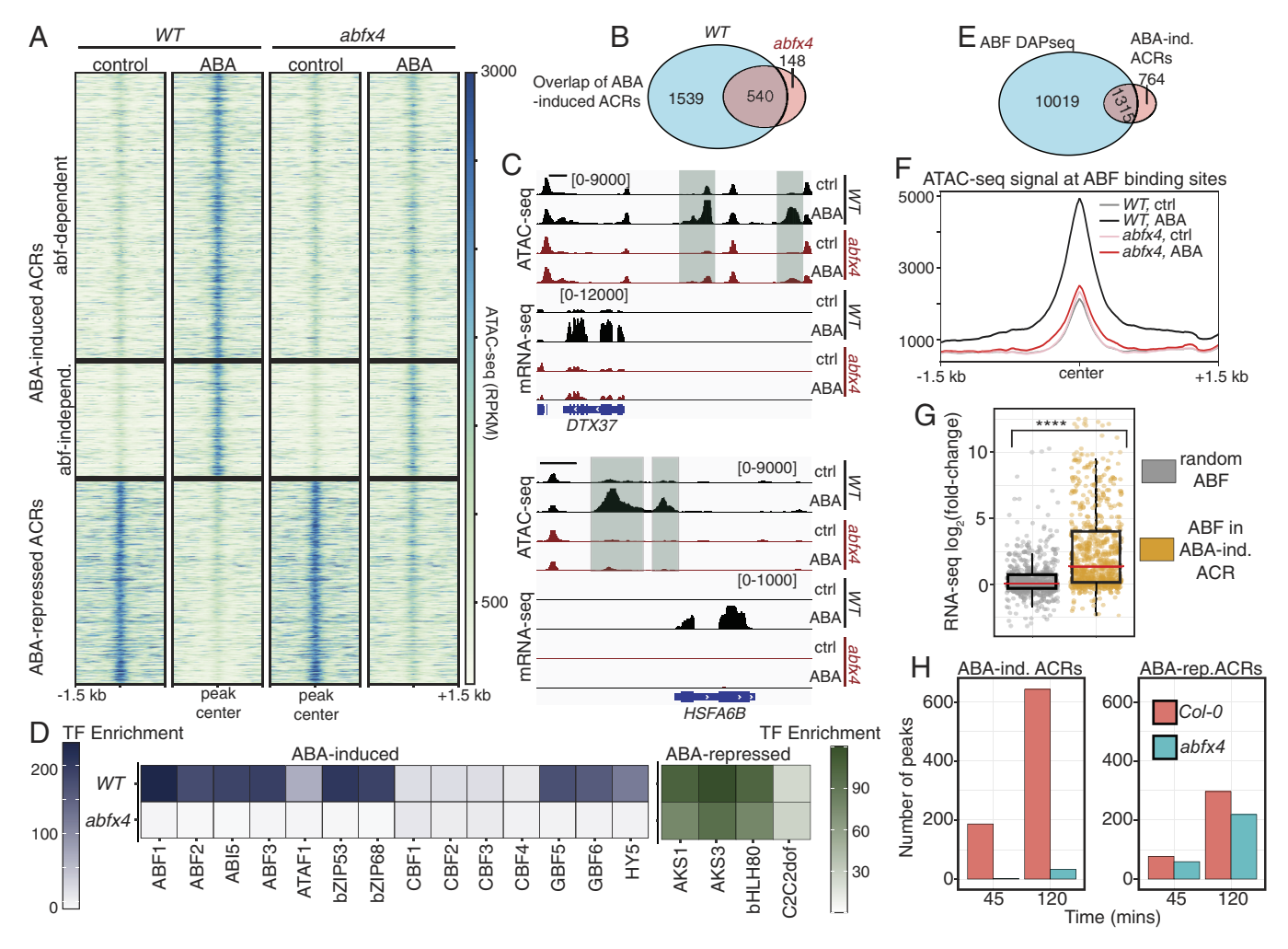


Fig. 4. ABF TFs are required for ABA-induced chromatin opening in guard cells. (A) Heatmaps of ATAC-seq signal (RPKM-normalized) in either WT or abfx4 mutant guard cells centered over 2,079 regions with ABA-induced accessibility and 975 regions with ABA-repressed accessibility (FDR < 0.001 and FC > 2.0). ACRs are subdivided by requirement for ABF1/2/3/4. (B) Overlap of ABA-induced ATAC-seq peaks in WT guard cells with those in abfx4 mutant guard cells. (C) Genome browser snapshots showing ATAC-seq and RNA-seq signal near two ABA-induced genes DTX37 and HSFA6B. (Scale bars indicate 1 kb.) (D) Enrichment [-log(P_value)] of the indicated TF binding motifs in ABA-regulated ATAC-seq peaks in either WT or abfx4 mutant guard cell nuclei. (E) Overlap between ABF DAP-seq peaks and ABA-induced ACRs. (F) Peak-centered metaplot showing ATAC-seq signal in the indicated samples at ABA-induced ACRs containing ABF DAP-seq binding sites. (G) 1,000 ABF DAP-seq peaks overlapping ABA-induced ATAC-seq peaks or 1,000 random ABF DAP-seq peaks were assigned to nearest downstream genes (within -2.5 kb and +0.5 kb of TSS). The boxplot shows the ABA-induced fold changes within these two sets of downstream transcripts. Asterisks (****) indicate that the distributions are significantly different by Welch's t test (P < 1E-7), and the red bars represent the means of the distributions. (H) Bar plots representing the number of ABA-activated or ABA-repressed ACRs over time in Col-0 or abfx4 mutant roots.

Fig. S10A, and Dataset S3). However, ABA repressed a similar number of root ACRs in the absence of ABF1/2/3/4 (Fig. 4H and SI Appendix, Fig. S10A). Although our data support a general requirement for ABFs in ABA-induced chromatin opening in roots and guard cells, we do find that some guard cell-specific ABA-induced ACRs are ABF-dependent (SI Appendix, Fig. S10 D and E). Collectively, these results demonstrate that the ABF1/2/3/4 TFs are required for triggering genome-wide chromatin opening in response to ABA.

ABA and Changes to Atmospheric CO₂ Concentration Induce Distinct Chromatin Remodeling Programs in Guard Cells. Because we observed that ABA has extensive effects on chromatin accessibility in guard cells, we wondered whether chromatin structure may respond to other stimuli that drive stomatal movements. Here, we focus on changes to atmospheric CO₂ concentration. Exposure of plants to low CO₂ stimulates stomatal opening while high CO₂ drives stomatal closure (Fig. 5A). The exact role of ABA signaling during CO₂-induced stomatal

responses is unclear and is a matter of some debate (63, 64, 66). Recent studies suggest that although high-CO₂-induced stomatal closure requires basal ABA signaling it does not involve further SnRK2 kinase activation (63, 64). Comparing how these signals impact genome activity could provide insight into whether and how the mechanisms underlying guard cell responses to ABA and CO₂ may differ.

To generate low and high CO₂ guard cell ATAC-seq libraries, we exposed 6-wk-old plants to either 100 ppm CO₂ or 1,000 ppm CO₂ for 4 h, two treatments that induce robust stomatal responses (Fig. 5*B*). Surprisingly, in contrast to the extensive effect of ABA on chromatin accessibility in guard cells (Fig. 5C), we observed smaller changes in response to low CO₂ (Fig. 5D), and minimal changes following treatment with high CO₂ (Fig. 5*E*). Following exposure of plants to 100 ppm CO₂, 329 ACRs gained accessibility and 487 ACRs lost accessibility while treatment with 1,000 ppm CO₂ induced only 11 ACRs and repressed 79 ACRs (Dataset S3). Heatmaps of ATAC-seq signal at ABA- and low CO₂-regulated regions highlighted the specificity of these

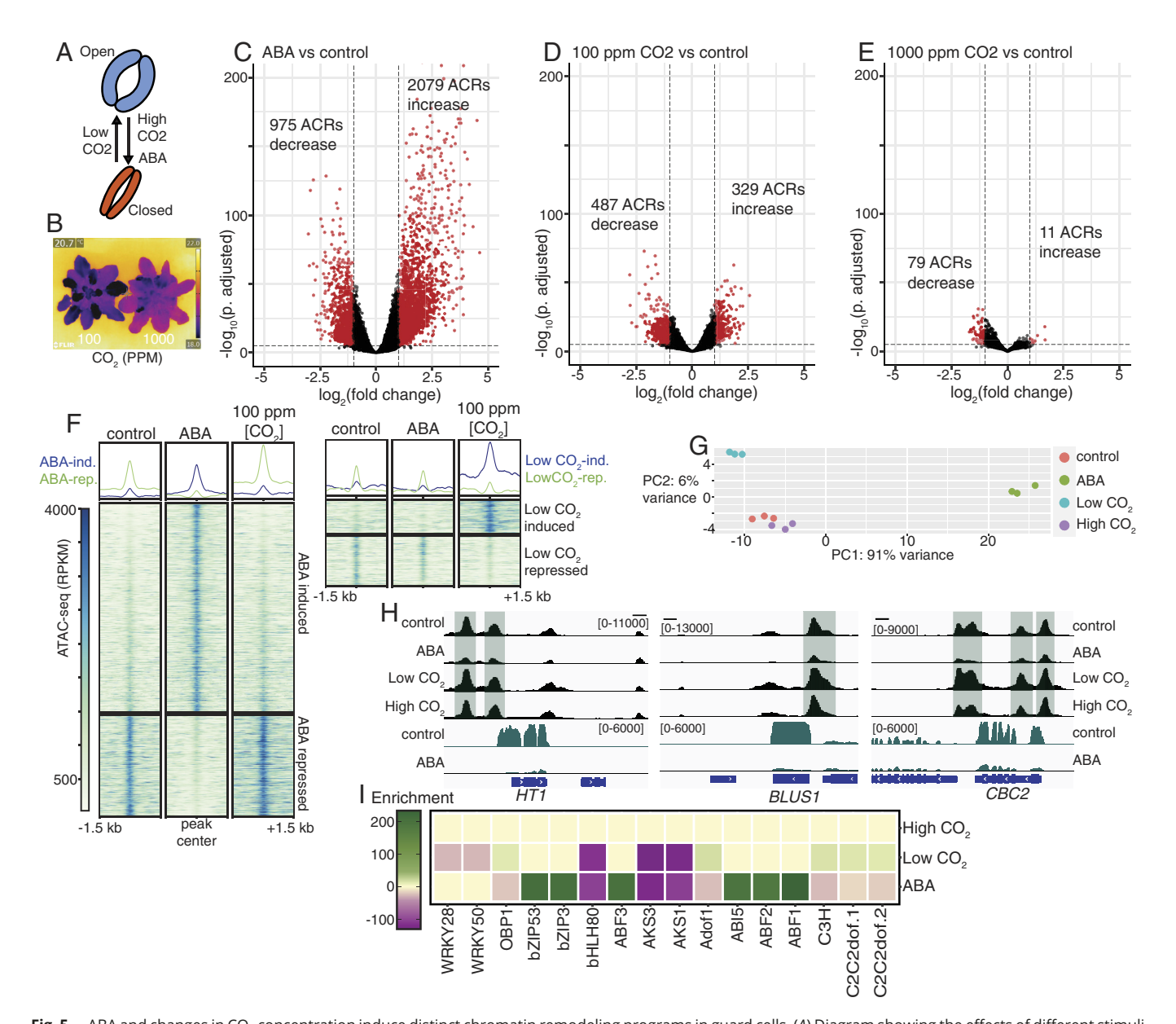


Fig. 5. ABA and changes in CO₂ concentration induce distinct chromatin remodeling programs in guard cells. (A) Diagram showing the effects of different stimuli on the stomatal aperture. (B) Representative IR image showing differences in leaf temperature due to CO2-induced stomatal movement. (C-E) Volcano plots of differential ATAC-seq results showing (C) ABA-regulated chromatin accessibility, (D) low CO₂-regulated chromatin accessibility, and (E) high CO2-regulated chromatin accessibility. The numbers of differentially accessible peaks (colored in red, FDR < 0.001 and FC > 2.0) in each condition are indicated on each plot. (F) Heatmaps and profile plots of guard cell ATAC-seq signal centered over either ABA-regulated ACRs (2,079 induced and 975 repressed) or low CO₂-regulated ACRs (329 induced and 487 repressed). Libraries are derived from plants exposed to the indicated treatments. (G) PCA shows that ABA, low CO₂, and high CO₂ introduce separate variation to genome-wide chromatin accessibility. (H) Genome browser images of guard cell ATAC-seq signal (in black) and RNA-seq signal (in green) among the indicated samples showing ABA-repression of chromatin accessibility upstream of HT1, BLUS1, and CBC1—three positive regulators of low CO₂ and blue light induced stomatal opening. (Scale bars indicate 1 kb.) (/) Enrichment (-log P_value) of the indicated TF binding motifs in ABA-, low CO₂-, or high CO₂-regulated regions. Negative enrichment scores indicate motifs overrepresented in treatment-represed regions. No significant enrichment for any of these motifs was found in high CO₂-regulated ACRs.

responses (Fig. 5F and SI Appendix, Fig. S7 A and B). PCA on our guard cell ATAC-seq datasets from different conditions further supports these findings and revealed little difference between control and high CO₂ treatments (Fig. 5G). Examination of individual loci highlights the specificity of these responses, for instance, chromatin opening upstream of ERF113 only occurred in response to ABA while the upstream region of the PP2C-encoding AT2G25070 gains accessibility only in response to low CO₂ (SI Appendix, Fig. S11 B–E).

Analysis of the set relationships among ABA-, low CO₂-, and high CO₂-regulated ACRs revealed little overlap suggesting that these stimuli control distinct CREs in the genome (SI Appendix, Fig. S11A). We did find overlap between ABA-induced and low

CO2-repressed ACRs and between ABA-repressed and low CO₂-induced ACRs. ABA-repressed regions had elevated average ATAC-seq signal in guard cells isolated from plants exposed to 100 ppm [CO₂] (Fig. 5F). For instance, ABA-repressed chromatin accessibility upstream of ALMT6 while low-CO2 treatment enhanced accessibility (SI Appendix, Fig. S11D). Interestingly, ABA repressed chromatin accessibility upstream of HT1, BLUS1, and CBC2 (67), all key positive regulators of low CO₂- and blue light-induced stomatal opening, while high CO2 had no effect (Fig. 5H). These data indicate that chromatin remodeling represents an important cross talk point for these stimuli, ensuring robust stomatal closing or opening, depending on the physiological conditions. DNA binding motif analysis further emphasized the distinct regulatory impacts of changes in CO2 concentration and ABA on the genome (Dataset S7). In contrast to our motif analysis on ABA-induced ACRs, we did not find enrichment of ABF binding motifs in low or high CO₂ regulated chromatin (Fig. 51). Instead, low CO₂ gained ACRs were enriched for motifs recognized by C2C2dof-type TFs which were oppositely enriched only in ABA-repressed ACRs. Collectively, our data demonstrate how different signals that control stomatal movement deploy distinct gene regulatory programs in guard cells.

Discussion

ABA triggers changes in gene expression, but whether this transcriptional response depends on chromatin remodeling has remained unknown (5). Here, we reveal massive ABA-induced chromatin remodeling pointing to an orchestrated reprogramming of the Arabidopsis epigenome by specific sets of TFs. We identify regulatory regions of the genome specifically active in guard cells and uncover how the accessibility of these sequences is modified by signals that control stomatal aperture size.

Guard cell regulation of stomatal aperture size is essential for plant survival under drought stress. Such regulation requires that the guard cells forming the stomatal pore integrate numerous physiological and environmental cues. In this study, we profiled genome-wide chromatin accessibility in tens of thousands of guard cells isolated from soil-grown plants exposed to different stimuli that trigger stomatal movements. Our results lead us to propose that guard cell ABA signaling controls the balance between two opposing chromatin states. Under unstressed conditions, AKS proteins maintain open chromatin at upstream regulatory regions of ABA-repressed genes while ABA-activated genes are kept silent by closed chromatin. Under abiotic stress such as drought, ABA levels rise in guard cells, thereby activating SnRK2 kinases which subsequently inhibit AKSs and activate ABFs. This leads to chromatin opening upstream of abiotic stress-activated genes and the loss of chromatin accessibility upstream of stress-repressed genes.

We uncovered patterns of chromatin accessibility specific to guard cells (Fig. 2D) and identified cis-regulatory regions supporting guard cell specific gene expression (Fig. 2 *F–I* and Dataset S4). We found that ABA induces extensive and cell type-specific chromatin remodeling and that guard cells possess a more extensive response than mesophyll and root cells (Fig. 3K and SI Appendix, Fig. S7 *C–L*). Importantly, we find that these ABA-induced chromatin remodeling events correlate with ABA-regulated gene expression (Fig. 3E and SI Appendix, Fig. S6C). By performing TF-binding motif enrichment and analyzing published DAP-seq data, we hypothesized that the bZIP TFs ABF1/2/3/4 may function in ABA-induced chromatin remodeling in guard cells (Fig. 3 C and G and SI Appendix, Fig. S6M). Interestingly, we find that among in vitro ABF binding sites, those occurring within ABA-opened chromatin are most strongly associated with ABA-induced transcription (Fig. 4G), indicating that regulated chromatin accessibility may determine which genomic ABF binding sites are functional. Our experiments in abf1/2/3/4 quadruple mutant guard cells demonstrate that these four TFs are essential for the majority of ABA-triggered chromatin opening (Fig. 4). Furthermore, experiments in root nuclei show that in abf1/2/3/4 quadruple mutants, even early ABA-induced chromatin remodeling events are strongly impaired (Fig. 4H and SI Appendix, Fig. S10), suggesting that ABFs initiate chromatin opening. How ABFs accomplish chromatin opening remains to be determined, but existing literature could be interpreted to support two possible and not necessarily mutually exclusive explanations. 1) Although nucleosomes can restrict TF binding to DNA, some TFs, known as pioneer factors (68, 69), possess the ability to bind their

target sequences even within in ACRs. At present, only a handful of pioneer factors have been documented in plants (70). While our data are consistent with ABFs acting as pioneer factors, future biochemical experiments reconstituting ABF binding to nucleosomal DNA are needed to investigate this model. 2) ABFs may recruit chromatin-modifying proteins to target sequences which could increase chromatin accessibility. Interestingly, several such molecules including the SWI/SNF ATPase BRM (71, 72) and the histone deacetylase HDA9 (73) interact with known ABA signaling components. Furthermore, ABF-binding proteins known as AFPs, which negatively regulate ABA signaling, have been shown to physically interact with histone and chromatin-modifying factors (74).

Although our data support a general requirement for ABF proteins in both roots and guard cells, we also observe that ABA alters chromatin accessibility in a cell type-specific manner. At present, we do not understand how ABFs might contribute to cell typespecific regulation of chromatin. Beyond ABF1/2/3/4, our analyses implicated additional TFs in ABA-dependent genome reprogramming (Fig. 3 F and G), which is consistent with prior research showing that ABA regulates the binding of multiple TFs (75). We observed that ~26% of ABA-gained ACRs (540 ACRs) still open in *abfx4* mutant guard cells in response to ABA (Fig. 4*B*). These ABF-independent regions retained enrichment for CBF1/2/3 binding motifs, suggesting that CBF TFs display ABF-independent binding (Fig. 4D). Finally, although ABA-induced chromatin opening is severely impaired in abf1/2/3/4 quadruple mutant guard cells, we cannot exclude the possibility that other ABRE-binding TFs, in particular ABI5 (76, 77), participate in this process as well.

Notably, our data suggest that the related bHLH TFs AKS1/2/3 play a larger role in the regulation of ABA-repressed genes than was previously thought. Prior research had shown that SnRK2 kinase-dependent inhibition of AKS1/2 was required for the ABA-dependent transcriptional repression of the K+ ion channel gene KAT1 in guard cells (24). Surprisingly, we found that AKS1 bound many regions in the genome that lose chromatin accessibility in guard cells following ABA treatment (Fig. 3C). Additionally, motifs recognized by AKS1/3 and the related protein bHLH80 were enriched in ABA-repressed ACRs in guard cells (Fig. 3H), as well as in root and mesophyll cells (Fig. 1*F*, *SI Appendix*, Fig. S3*G*, and Dataset S7). This observation was further supported by de novo motif analysis (SI Appendix, Fig S6N). AKS1 and AKS2 are inhibited by direct ABA-dependent SnRK2 phosphorylation, but their expression was not controlled by ABA signaling (44). We found that in guard cells, ABA represses AKS3 expression implying that ABA-dependent inhibition of AKS proteins occurs through both transcriptional and phosphorylation-dependent mechanisms (Fig. 3 *I* and *J*).

Elevation in the CO₂ concentration in leaves triggers rapid stomatal closing (34). The extent to which elevated atmospheric CO₂ signals through the ABA signal transduction pathway is currently under debate. Different research groups using the same mutants have come to different conclusions regarding direct CO2 signaling via the early ABA receptor/SnRK2 kinase pathway during CO₂-induced stomatal closure. Our results expose major differences in how guard cells interpret these stimuli. In contrast to the extensive and persistent changes to chromatin structure induced by ABA (Fig. 3), exposure to elevated CO₂ had minimal impact on genome-wide chromatin accessibility in guard cells (Fig. 5). While ABA controlled chromatin accessibility at 3,018 ACRs in the genome, we found that only 90 ACRs were regulated by elevated CO₂ (Fig. 5 C-E). Additionally, the strong enrichments of ABF binding motifs in gained ACRs and AKS binding motifs in lost ACRs, evident following ABA treatment, are absent during the response to elevated CO₂ (Fig. 51). The disparity

between these two signals at the level of chromatin mirrors the disparity between characteristics of their respective physiological responses. Unlike ABA- and drought-triggered stomatal closure, elevated CO₂-induced stomatal closure is rapidly reversed upon return to ambient CO₂ (63). Such rapid changes in the intercellular CO2 concentration in leaves occur for example with alternating light intensities (e.g., passing cloud cover) and require rapid reversals of stomatal CO₂ responses. Furthermore, we found that exposure to low CO₂ triggers a distinct program of chromatin remodeling in guard cells (Fig. 5 *F–I*).

Finally, our results may open broad avenues for investigation into two poorly understood features of stomatal biology. Studies in multiple plant species have documented a phenomenon referred to as stomatal "memory" (78, 79). Following drought stress and rewatering, plants typically exhibit delayed and/or slow reopening of stomata despite rapid recovery of plant water status. Furthermore, guard cells display transcriptional memory where repetitive dehydration stress leads to altered transcript levels in subsequent stress events (80–82). We found that ABA triggered changes to chromatin accessibility in guard cells that can persist for up to 24 h, which could prime the genome for subsequent abiotic stress exposure (Fig. 3). These shifts occurred at thousands of locations in the genome including upstream of many genes known to regulate stomatal movements as well as many genes with potential functions in stomatal physiology that could be the basis for future studies (SI Appendix, Fig. S6 and Dataset S3). Moreover, our findings support cross talk between ABA and low CO₂ signaling at the chromatin remodeling level. For example, we uncovered that ABA, but not high CO₂, triggered chromatin closing upstream of genes encoding key CO₂-sensing and signaling proteins that promote low CO₂-induced stomatal opening, including HT1, BLUS1, and CBC2 (Fig. 5H). This response may contribute to the long-term stomatal closing triggered by drought and ABA by inhibiting mechanisms for low CO₂-induced stomatal opening. ABA-triggered chromatin dynamics may provide a basis for long-term reprogramming of the guard cell genome for abiotic stress survival. We envision that these sustained changes to chromatin structure may store the experience of drought stress and contribute to long-term adjustments of stomatal function.

Methods

Plant Material and Growth Conditions. The Columbia-0 (Col-0) accession of A. thaliana was used as the wild-type background. Experiments on seedlings were conducted using plants germinated and grown on 1/2 Murashige and Skoog (MS) media (pH 5.7 to 8) solidified with 1% Phyto-agar. Experiments on mature plants were conducted using plants grown in soil (Sunshine Mix #1) filled plastic pots incubated in a growth chamber (Conviron) under a 12 h-12 h light-dark cycle, a light intensity of 100 μ mol m⁻² s⁻¹, a temperature of 22 °C, ambient [CO₂], and a relative humidity of 65%. To minimize the impact of environmental variation, all experiments were performed on plants grown in two identical growth chambers equipped with [CO₂] control.

ABA treatments in plate-based experiments were performed using a mesh (100 µm polyester) transfer method. Seeds were germinated on ½ MS agar plates overlaid with sterilized polyester mesh (100 µm). ABA treatments were initiated by transferring 8-d-old seedlings in mass to plates containing 50 μM ABA (Sigma cis/trans-ABA) or to plates containing vehicle control (Ethanol). ABA treatments on soil-grown plants were performed by spraying plants with 50 μM ABA diluted with 0.01% Silwet (in water) or with vehicle control. To assess treatment responses, leaf temperature was measured using an infrared thermal imaging camera (T650sc; FLIR).

Plasmid DNA and Plant Transformation. Constructs for cell type-specific nuclear sorting were prepared using multisite gateway technology (Invitrogen). The Open Reading Frame (ORF) encoding the histone H2B (AT5G22880) was cloned in a pDONR221 entry vector. The cell type-specific promotors RBCp and GC1p, from the Rubisco small subunit 2B gene (AT5G38420) and the GASA9

(AT1G22690) gene, respectively, were cloned from the Arabidopsis genome into the gateway entry vector pDONR-p4p1r. Final plant transformation constructs were generated by performing multisite gateway recombination into the pP7m34GW destination vector. The plasmid for expressing GFP-AKS3 under the AKS3 (AT2G42280) endogenous promotor was generated using GreenGate cloning (83). The cloned AKS3 upstream regulatory sequence was defined using guard cell ATAC-seq data. Transcriptional reporter constructs expressing nuclear-localized GFP under the guard cell-specific ACRs upstream of AAE9 (AT1G21540) and ALMT6 (AT2G17470) were generated using GreenGate cloning. Primer sequences are available in Dataset S8. Constructs were transformed into A. thaliana Col-O plants using floral dipping with Agrobacterium tumefaciens strain GV3101.

FANS. FANS on seedling/root nuclei and mesophyll nuclei was performed similar to a previous study (40) with small modifications. Briefly, whole seedlings, surgically isolated roots, or leaves were chopped vigorously with a clean razor blade in 2 to 3 mL of ice-cold FANS-lysis buffer (15 mM Tris-HCl pH7.5, 20 mM NaCl, 80 mM KCl, 0.2 mM spermine, 5 mM 2-ME, 0.5 mM spermidine, 0.2% IGEPAL CA-630, and Roche mini EDTA-free Protease Inhibitor Cocktail) for 5 min in a cold glass petri dish. The subsequent lysate was filtered through a 40-µm filter unit before transferring to a 15-mL tube containing 3 mL of FANS-Sucrose buffer (20 mM Tris-HCl pH 8.0, 2 mM MgCl₂, 2 mM EDTA, 15 mM 2-ME, 1.7 M sucrose, and 0.2% IGEPAL CA-630). Nuclei were pelleted at 2,500 \times G at 4 °C for 25 min, after which the supernatant was carefully removed. The nuclei pellet was then gently resuspended, using clipped pipette tips, with 600 µL FANS-lysis buffer supplemented with DAPI, and then immediately used for flow cytometry.

For experiments on quard cells, the leaves of ~40 six-week-old plants were harvested and blended in 500 mL of ice-cold water for 2 \times 40 s with 1 min between pulses. The blended sample was poured over a 100-µm mesh to remove mesophyll cells and collect epidermal-enriched fragments. The mesh was rinsed with ~200 mL of cold water and gently blotted with paper towels to remove excess liquid. Thin sections of epidermal tissue were then flash-frozen in liquid nitrogen. Epidermal sections were ground to a fine powder with a frozen mortar and pestle. After grinding, powder was transferred to a new mortar with a frozen metal spatula. Immediately, 12 to 15 mL of ice-cold FANS-lysis buffer was added, and the powder was gently resuspended with a clean pestle. The subsequent lysate was filtered through a 40-µm filter unit before transferring to a 15-mL tube containing 6 mL of FANS-Sucrose buffer. Nuclei were then pelleted and prepared for FACS as above.

Flow cytometry was conducted on a BD FACS Aria II using a $70\text{-}\mu\text{m}$ nozzle with a flow rate <2 and the following photomultiplier parameters: Forward Scatter (FSC)-250 eV, Side Scatter (SSC)-220 eV, BV421 (DAPI channel)-550 eV, and FITC (GFP channel)-340 eV. Sort gates were defined empirically using the FSC and SSC channels to exclude debris and potential doublets. Before sorting GFP-labeled nuclei, FACS analysis on unlabeled control samples (Col-0 nuclei) was performed to define background fluorescence signal. When isolating guard cell nuclei, sort gates were established to purify exclusively 2N (diploid) and GFP-positive nuclei. To evaluate the purity of sorted samples, a fraction (~10% of total volume) was rerun under the same sorting program (SI Appendix, Fig. S2D). Sorted nuclei were collected in 600 μL of FANS-lysis buffer in a refrigerated tube chamber. After sorting, nuclei were pelleted by centrifugation at 1,000 × g for 10 min at 4 °C. Nuclei pellets were gently washed with 1 mL of 10 mM Tris-HCl pH 8.0 and 5 mM MgCl2 buffer before centrifugation again as above. After carefully removing the supernatant, nuclei were used immediately for ATAC-seq.

Detailed methods descriptions for microscopy and time-resolved stomatal conductance measurements can be found in SI Appendix, Materials and Methods. Detailed protocols for RNA-seq and ATAC-seq library preparation and description of ATAC-seq, RNA-seq, and DAP-seq data analyses can be found in SI Appendix, Materials and Methods.

Data and materials availability. All materials (plasmids and seed stocks) are available upon request. Raw FASTO files generated in this study and ATAC-seq peak files in narrowPeak format are available at NCBI's Gene Expression Omnibus under accession number GSE243473 (84). All data are available in the main text and supporting information.

ACKNOWLEDGMENTS. Funding for this study was provided by the NIH (R01GM060396 to J.I.S and F32GM137544 to C.A.S). CO₂ experiments were supported by NSF grant MCB-1900567 to J.I.S. This study includes data generated at the UC San Diego IGM Genomics Center utilizing an Illumina NovaSeq 6000 that was purchased with funding from a NIH SIG grant (#S10

- OD026929). Microscopy was supported by the UC San Diego Microscopy Core with funding by grant NINDS P30NS047101. We thank Kazuko Yamaguchi-Shinozaki (University of Tokyo) for sharing abf1/2/3/4 quadruple mutant seeds and members of the Schroeder lab for helpful discussions throughout the research.
- R. J. Schmitz, E. Grotewold, M. Stam, Cis-regulatory sequences in plants: Their importance, discovery, and future challenges. *The Plant Cell* **34**, 718-741 (2022).
 W. K. M. Lai, B. F. Pugh, Understanding nucleosome dynamics and their links to gene expression
- and DNA replication. Nat. Rev. Mol. Cell Biol. 18, 548-562 (2017).
- T. C. Voss, G. L. Hager, Dynamic regulation of transcriptional states by chromatin and transcription factors. Nat. Rev. Genet. 15, 69-81 (2014).
- J. L. Nemhauser, F. Hong, J. Chory, Different plant hormones regulate similar processes through largely nonoverlapping transcriptional responses. Cell 126, 467-475 (2006).
- R. Waadt et al., Plant hormone regulation of abiotic stress responses. Nat. Rev. Mol. Cell Biol. 23,
- P. Sijacic, M. Bajic, E. C. McKinney, R. B. Meagher, R. B. Deal, Changes in chromatin accessibility between Arabidopsis stem cells and mesophyll cells illuminate cell type-specific transcription factor networks. Plant J. 94, 215-231 (2018).
- K. A. Maher et al., Profiling of accessible chromatin regions across multiple plant species and cell types reveals common gene regulatory principles and new control modules. The Plant Cell 30, 15-36 (2018).
- A. M. Sullivan *et al.*, Mapping and dynamics of regulatory DNA in maturing Arabidopsis thaliana siliques. *Front. Plant Sci.* **10**, 1434 (2019).
- A. Farmer, S. Thibivilliers, K. H. Ryu, J. Schiefelbein, M. Libault, Single-nucleus RNA and ATAC sequencing reveals the impact of chromatin accessibility on gene expression in Arabidopsis roots at the single-cell level. Mol. Plant 14, 372-383 (2021).
- M. Borg et al., Epigenetic reprogramming rewires transcription during the alternation of generations in Arabidopsis. eLife 10, e61894 (2021).
- A. P. Marand, Z. Chen, A. Gallavotti, R. J. Schmitz, A cis-regulatory atlas in maize at single-cell resolution. Cell 184, 3041-3055.e21 (2021).
- E.-D. Kim et al., Dynamic chromatin accessibility deploys heterotypic cis/trans-acting factors driving stomatal cell-fate commitment. Nat. Plants 8, 1453-1466 (2022).
- 13. K. C. Potter, J. Wang, G. E. Schaller, J. J. Kieber, Cytokinin modulates context-dependent chromatin accessibility through the type-B response regulators. Nat. Plants 4, 1102-1111 (2018).
- 14. M. A. Reynoso et al., Evolutionary flexibility in flooding response circuitry in angiosperms. Science 365, 1291-1295 (2019).
- E. S. Karaaslan, N. Faiß, C. Liu, K. W. Berendzen, Isolation of lineage specific nuclei based on distinct endoreduplication levels and tissue-specific markers to study chromatin accessibility landscapes. Plants 9, 1478 (2020).
- S. R. Cutler, P. L. Rodriguez, R. R. Finkelstein, S. R. Abrams, Abscisic acid: Emergence of a core signaling network. Ann. Rev. Plant Biol. 61, 651-679 (2010).
- R. Finkelstein, Abscisic acid synthesis and response. Arabidopsis Book 11, e0166 (2013).
- J.-K. Zhu, Abiotic stress signaling and responses in plants. Cell 167, 313-324 (2016).
- Y. Ma et al., Regulators of PP2C phosphatase activity function as abscisic acid sensors. Science 324, 1064-1068 (2009).
- S.-Y. Park et al., Abscisic acid inhibits type 2C Protein phosphatases via the PYR/PYL family of START proteins. Science 324, 1068-1071 (2009).
- T. Umezawa et al., Type 2C protein phosphatases directly regulate abscisic acid-activated protein kinases in Arabidopsis. Proc. Natl. Acad. Sci. U.S.A. 106, 17588-17593 (2009).
- H. Fujii, P. E. Verslues, J.-K. Zhu, Identification of two protein kinases required for abscisic acid regulation of seed germination, root growth, and gene expression in Arabidopsis. The Plant Cell 19, 485-494 (2007).
- 23. K. E. Hubbard, N. Nishimura, K. Hitomi, E. D. Getzoff, J. I. Schroeder, Early abscisic acid signal transduction mechanisms: Newly discovered components and newly emerging questions. Genes. Dev. 24, 1695-1708 (2010).
- $Y. Takahashi\ \textit{et\ al.}, b HLH\ transcription\ factors\ that\ facilitate\ K+\ uptake\ during\ stomatal\ opening\ are$ repressed by abscisic acid through phosphorylation. Sci. Signaling 6, ra48 (2013).
- T. Yoshida et al., AREB1, AREB2, and ABF3 are master transcription factors that cooperatively regulate ABRE-dependent ABA signaling involved in drought stress tolerance and require ABA for full activation. Plant J. 61, 672-685 (2010).
- T. Yoshida et al., Four Arabidopsis AREB/ABF transcription factors function predominantly in gene expression downstream of SnRK2 kinases in abscisic acid signalling in response to osmotic stress. Plant Cell Environ. 38, 35-49 (2015).
- 27. P. Wang et al., Quantitative phosphoproteomics identifies SnRK2 protein kinase substrates and reveals the effectors of abscisic acid action. Proc. Natl. Acad. Sci. U.S.A. 110, 11205-11210 (2013).
- T. Umezawa et al., Genetics and phosphoproteomics reveal a protein phosphorylation network in the abscisic acid signaling pathway in Arabidopsis thaliana. Sci. Signal. 6, rs8 (2013).
- N. Leonhardt et al., Microarray expression analyses of Arabidopsis guard cells and isolation of a recessive abscisic acid hypersensitive protein phosphatase 2C mutant. The Plant Cell 16, 596-615 (2004).
- H. Goda *et al.*, The AtGenExpress hormone and chemical treatment data set: Experimental design, data evaluation, model data analysis and data access. *Plant J.* **55**, 526–542 (2008).
- R.-S. Wang et al., Common and unique elements of the ABA-regulated transcriptome of Arabidopsis guard cells. BMC Genom. 12, 216 (2011).
- Å. M. Hetherington, F. I. Woodward, The role of stomata in sensing and driving environmental change. Nature 424, 901-908 (2003).
- S. M. Assmann, T. Jegla, Guard cell sensory systems: Recent insights on stomatal responses to light, abscisic acid, and CO2. Curr. Opin. Plant Biol. 33, 157-167 (2016).
- G. Dubeaux et al., Deep dive into CO2-dependent molecular mechanisms driving stomatal responses in plants. Plant Physiol. 187, 2032-2042 (2021).
- Z. Liu et al., Global dynamic molecular profiling of stomatal lineage cell development by single-cell RNA sequencing. Mol. Plant 13, 1178-1193 (2020).
- C. B. Lopez-Anido et al., Single-cell resolution of lineage trajectories in the Arabidopsis stomatal lineage and developing leaf. Dev. Cell 56, 1043–1055.e4 (2021).

- 37. J.-Y. Kim et al., Distinct identities of leaf phloem cells revealed by single cell transcriptomics. The Plant Cell 33, 511-530 (2021).
- C. Procko et al., Leaf cell-specific and single-cell transcriptional profiling reveals a role for the palisade layer in UV light protection. Plant Cell **34**, 3261–3279 (2022).
- J. D. Buenrostro, P. G. Giresi, L. C. Zaba, H. Y. Chang, W. J. Greenleaf, Transposition of native chromatin for fast and sensitive epigenomic profiling of open chromatin, DNA-binding proteins and nucleosome position. *Nat. Methods* **10**, 1213–1218 (2013).
- 40. Z. Lu, B. T. Hofmeister, C. Vollmers, R. M. DuBois, R. J. Schmitz, Combining ATAC-seq with nuclei sorting for discovery of cis-regulatory regions in plant genomes. Nucleic Acids Res. 45, e41 (2017).
- A. M. Jones et al., Abscisic acid dynamics in roots detected with genetically encoded FRET sensors. eLife 3, e01741 (2014).
- 42. R. Waadt et al., FRET-based reporters for the direct visualization of abscisic acid concentration changes and distribution in Arabidopsis. eLife 3, e01739 (2014).
- R. C. O'Malley et al., Cistrome and epicistrome features shape the regulatory DNA landscape. Cell **165**, 1280-1292 (2016).
- Y. Takahashi, T. Kinoshita, M. Matsumoto, K. Shimazaki, Inhibition of the Arabidopsis bHLH transcription factor by monomerization through abscisic acid-induced phosphorylation. Plant J. 87, 559-567 (2016).
- Y. Yang, A. Costa, N. Leonhardt, R. S. Siegel, J. I. Schroeder, Isolation of a strong Arabidopsis guard cell promoter and its potential as a research tool. Plant Methods 4, 6 (2008).
- J. A. Anderson, S. S. Huprikar, L. V. Kochian, W. J. Lucas, R. F. Gaber, Functional expression of a probable Arabidopsis thaliana potassium channel in Saccharomyces cerevisiae. Proc. Natl. Acad. Sci. U.S.A. 89, 3736-3740 (1992).
- 47. D. P. Schachtman, J. I. Schroeder, W. J. Lucas, J. A. Anderson, R. F. Gaber, Expression of an inwardrectifying potassium channel by the Arabidopsis KAT1 cDNA. Science 258, 1654-1658 (1992).
- R. L. Nakamura et al., Expression of an Arabidopsis potassium channel gene in guard cells. Plant Physiol. 109, 371-374 (1995).
- O. S. Lau et al., Direct roles of SPEECHLESS in the specification of stomatal self-renewing cells. Science 345, 1605-1609 (2014).
- S.-K. Han et al., MUTE directly orchestrates cell-state switch and the single symmetric division to create stomata. Dev. Cell 45, 303-315.e5 (2018).
- K. Ohashi-Ito, D. C. Bergmann, Arabidopsis FAMA controls the final proliferation/differentiation switch during stomatal development. *The Plant Cell* **18**, 2493–2505 (2006).
- H. Yu et al., Activated expression of an Arabidopsis HD-START protein confers drought tolerance with improved root system and reduced stomatal density. The Plant Cell 20, 1134–1151 (2008).
- J. Negi et al., A dof transcription factor, SCAP1, is essential for the development of functional stomata in Arabidopsis. Curr. Biol. 23, 479-484 (2013).
- S. Meyer et al., Malate transport by the vacuolar AtALMT6 channel in guard cells is subject to multiple regulation. Plant J. 67, 247-257 (2011).
- S. Li et al., Arabidopsis ACYL-ACTIVATING ENZYME 9 (AAE9) encoding an isobutyl-CoA synthetase is a key factor connecting branched-chain amino acid catabolism with iso-branched wax biosynthesis. New Phytol. 233, 2458-2470 (2022).
- E. Cominelli et al., A quard-cell-specific MYB transcription factor regulates stomatal movements and plant drought tolerance. Curr. Biol. 15, 1196-1200 (2005).
- M. Hashimoto et al., Arabidopsis HT1 kinase controls stomatal movements in response to CO2. Nat. Cell Biol. 8, 391-397 (2006).
- Y.-K. Liang et al., AtMY861, an R2R3-MYB transcription factor controlling stomatal aperture in Arabidopsis thaliana. *Curr. Biol.* **15**, 1201–1206 (2005). 58.
- M. B. Prouse, M. M. Campbell, Interactions between the R2R3-MYB transcription factor, AtMYB61, and target DNA binding sites. PLoS One 8, e65132 (2013).
- $S.\,J.\,Gilmour\,\textit{et al.}, Low\,temperature\,regulation\,of\,the\,Arabidopsis\,CBF\,family\,of\,AP2\,transcriptional$ activators as an early step in cold-induced COR gene expression. Plant J. 16, 433-442 (1998).
- S. Heinz et al., Simple combinations of lineage-determining transcription factors prime cisregulatory elements required for macrophage and B cell identities. Mol. Cell 38, 576-589 (2010).
- W. Lahr, K. Raschke, Abscisic-acid contents and concentrations in protoplasts from guard cells and mesophyll cells of Vicia faba L. Planta 173, 528-531 (1988).
- P.-K. Hsu et al., Abscisic acid-independent stomatal CO2 signal transduction pathway and convergence of CO2 and ABA signaling downstream of OST1 kinase. Proc. Natl. Acad. Sci. U.S.A. 115,
- E9971-E9980 (2018). 64. L. Zhang et al., FRET kinase sensor development reveals SnRK2/OST1 activation by ABA but not by
- MeJA and high CO2 during stomatal closure. *eLife* **9**, e56351 (2020).

 Y. Sun *et al.*, Divergence in the ABA gene regulatory network underlies differential growth control. *Nat. Plants* **8**, 549-560 (2022).
- M. Dittrich *et al.*, The role of Arabidopsis ABA receptors from the PYR/PYL/RCAR family in stomatal acclimation and closure signal integration. *Nat. Plants* **5**, 1002–1011 (2019).
- A. Hiyama et al., Blue light and CO2 signals converge to regulate light-induced stomatal opening. Nat. Commun. 8, 1284 (2017).
- M. Iwafuchi-Doi, K. S. Zaret, Pioneer transcription factors in cell reprogramming. Genes. Dev. 28, 2679-2692 (2014).
- A. Balsalobre, J. Drouin, Pioneer factors as master regulators of the epigenome and cell fate. Nat. Rev. Mol. Cell Biol. 23, 449-464 (2022).
- R. Jin et al., LEAFY is a pioneer transcription factor and licenses cell reprogramming to floral fate. Nat. Commun. 12, 626 (2021).
- S.-K. Han et al., The SWI2/SNF2 chromatin remodeling ATPase BRAHMA represses abscisic acid responses in the absence of the stress stimulus in Arabidopsis. The Plant Cell 24, 4892-4906 (2012).
- M. Peirats-Llobet et al., A direct link between abscisic acid sensing and the chromatin-remodeling ATPase BRAHMA via Core ABA signaling pathway components. Mol. Plant 9, 136-147 (2016).

- 73. D. Baek et al., Histone deacetylase HDA9 with ABI4 contributes to abscisic acid homeostasis in
- drought stress response. *Front. Plant Sci.* **11**, 143 (2020). T. J. Lynch, B. J. Erickson, D. R. Miller, R. R. Finkelstein, ABIS-binding proteins (AFPs) alter transcription of ABA-induced genes via a variety of interactions with chromatin modifiers. Plant Mol. Biol. 93, 403-418 (2017).
- L. Song et al., A transcription factor hierarchy defines an environmental stress response network. Science 354, 1550 (2016).
- R. Finkelstein, S. S. L. Gampala, T. J. Lynch, T. L. Thomas, C. D. Rock, Redundant and distinct functions of the ABA response loci ABA-INSENSITIVE(ABI)5 and ABRE-BINDING FACTOR (ABF)3. *Plant Mol. Biol.* **59**, 253-267 (2005).
- 59, 253-267 (2003).
 R. R. Finkelstein, T. J. Lynch, The Arabidopsis abscisic acid response gene ABI5 encodes a basic leucine zipper transcription factor. *The Plant Cell* 12, 599-609 (2000).
 E. Fleta-Soriano, M. Pintó-Marijuan, S. Munné-Bosch, Evidence of drought stress memory in the facultative CAM, Aptenia cordifolia: Possible role of phytohormones. *PLoS One* 10, e0135391 (2015).
- 79. P. A. Auler, F. B. S. Freire, V. F. Lima, D. M. Daloso, On the role of guard cells in sensing environmental signals and memorising stress periods. Theor. Exp. Plant Physiol. 34, 277-299 (2022).
- Y. Ding, M. Fromm, Z. Avramova, Multiple exposures to drought "train" transcriptional responses in Arabidopsis. Nat. Commun. 3, 740 (2012).
- 81. L. Virlouvet, M. Fromm, Physiological and transcriptional memory in guard cells during repetitive dehydration stress. New Phytol. 205, 596-607 (2015).
- denydration stress. New Phytol. 205, 596-607 (2015).
 A. van Weringh, A. Pasha, E. Esteban, P.J. Gamueda, N.J. Provart, Generation of guard cell RNA-seq transcriptomes during progressive drought and recovery using an adapted INTACT protocol for Arabidopsis thaliana shoot tissue. biorXiv [Preprint] (2021). https://doi.org/10.1101/2021.04.15.439991 (Accessed 10 June 2023).
 A. Lampropoulos et al., GreenGate-A novel, versatile, and efficient cloning system for plant transgenesis. PLoS One 8, e83043 (2013).
 C. A. Seller, J. L. Schwader, Dictingt award calls are if the compact for the provided of the property of the provided and pr
- C. A. Seller, J. I. Schroeder, Distinct guard cell specific remodeling of chromatin accessibility during abscisic acid and CO2 dependent stomatal regulation. Gene Expression Omnibus. https://www.ncbi.nlm.nih.gov/geo/query/acc.cgi?&acc=GSE243473. Accessed 12 November 2023.



Supporting Information for

Distinct guard cell-specific remodeling of chromatin accessibility during abscisic acid- and CO₂-dependent stomatal regulation

Authors

Charles A. Seller^{1*} and Julian I. Schroeder^{1*}

Affiliations

School of Biological Sciences
 Cell and Developmental Biology Department
 University of California San Diego,
 La Jolla, CA 92093-0116
 *Corresponding authors. Email: cseller@ucsd.edu; jischroeder@ucsd.edu

This PDF file includes:

Supporting text Figures S1 to S11 Legends for Datasets S1 to S8 SI References

Other supporting materials for this manuscript include the following:

Datasets S1 to S8

Supporting Information Text Extended Materials and Methods

Microscopy

Plant leaves were mounted on conventional glass microscope slides in water with the abaxial epidermal layer against the coverslip. GFP and chlorophyll fluorescence signals were recorded using either an Eclipse TE2000-U (Nikon, Tokyo, Japan) spinning disc confocal microscope or a Leica SP8 confocal microscope (Leica Microsystems). Constant gain, laser power, and exposure times were used for each experiment when comparing treatments/samples. On the Leica SP8 images were acquired using a 512 x 512 pixel resolution and a scan speed of 400 Hz. Displayed images are representative of at least 4 different leaves harvested from two independent transgenic lines. Images were processed for publication using Fiji software. 3D reconstructions from confocal imaging data were generated using Leica LAS X Software.

Time resolved stomatal conductance measurements

For gas exchange experiments, *Col-0* and *abfx4* mutant plants were grown together in the same growth chamber to minimize biological variation. Intact leaves of six-week-old plants were used for gas exchange experiments. Stomatal conductance was measured using a Licor-6400 infrared gas exchange analyzer equipped with a leaf chamber (LI-COR Biosciences). Before beginning measurements, clamped leaves were equilibrated for 45-60 mins at 150 µmol m⁻² s⁻¹ light intensity, ~65% relative humidity, 21°C, 400 ppm [CO₂], and an air flow of 400 µmol s⁻¹. Stomatal conductance was recorded every 30 seconds for a total of 30 min. To control for the effect of the diurnal rhythm on stomatal physiology, gas exchange experiments began 2 hours after the beginning of the light cycle and measurements were made alternating between different genotypes. Data are presented as average stomatal conductance +/- standard error of 5 plants per genotype.

RNA-seq

For whole leaf RNA-seq, total RNA was extracted from the leaves from 6 plants per sample using the Spectrum total RNA isolation kit. For guard cell enriched RNA-seq, the leaves of 20 plants per sample were blended for 30 sec in ice-cold water, filtered through a 100 µm mesh, and then blended and filtered again as above to isolate epidermal tissue. Thin sections of epidermal tissue were then frozen in liquid nitrogen and ground to a fine powder using a mortar and pestle. Total RNA was then extracted from ground tissue powder using the Qiagen RNeasy mini kit with oncolumn DNasel digestion. mRNA-seq libraries were prepared and sequenced on a NovaSeq 6000 (PE100) at the UCSD Institute for Genomic Medicine.

Following sequencing, adapter trimming and quality control checks were performed using Trim Galore version 0.6.5 (Cutadapt and FastQC). Reads were aligned to the *Arabidopsis thaliana* genome (TAIR10) using the Rsubread (version 2.14.0) *align* function (1). Low quality alignments (mapping quality < 2) were removed using the Samtools *view* function (version 1.17) (2). RNA-seq reads per transcript were counted to generate count matrices using the Rsubread *featureCounts* function. Differential expression analysis was performed using DESeq2 (version 1.26.0) (3). Transcripts were defined as significantly differentially expressed using the following thresholds: P adjusted value < 0.001 and fold change > 2. To visualize data using the Integrated Genomics Viewer (IGV) browser, bigwig coverage tracks were generated using the deepTools (version 3.5.0) *bamCoverage* function (bin size of 1 bp and normalization by Reads Per Kilobase per Million mapped reads - RPKM) (4). Gene ontology (GO) term enrichment analyses were performed with the Panther system and by applying a binomial test with p-values adjusted for multiple testing by a Bonferroni correction (5).

ATAC-seq

ATAC-seq was performed as described in (6). Sorted nuclei were resuspended in 40 µl of tagmentation reaction mixture (20 µl 2xTD buffer, 0.4 µl 10% Tween, 0.4 µl 1% digitonin, 13.2 µl 1xPBS, X µl H2O) supplemented with TDE1 enzyme (Illumina) at a ratio of 2.0 µl TDE1:50,000

nuclei. Reactions were incubated at 37°C for 30 mins. After incubation, tagmented DNA fragments were purified using the Qiagen min-Elute DNA kit with an elution volume of 22 µl. The entire volume of eluted tagmented DNA fragments was used to construct ATAC-seq libraries. ATAC-seq libraries were amplified with dual indexed Nextera primers using the NEBNext 2xHiFi PCR Master Mix (New England Biolabs) for 5 initial cycles. The number of additional amplification cycles was determined empirically by performing qPCR on 10% of the amplified library. Amplified libraries were then dual size selected using a 0.6x-1.2X ratio of SPRIselect magnetic beads (Beckman Coulter) and library quality was assessed by running samples on a HSD1000 ScreenTape on a Tapestation system (Agilent). ATAC-seq libraries were pooled at equimolar ratios and sequenced on a NovaSeq 6000 (PE150 mode) by Novogene.

To control for differences in data analysis between studies, previously published Mesophyll cell ATAC-seg raw FASTQ files were downloaded from SRA (SRP113667) and reanalyzed. Raw ATAC-seg sequence files were subjected to adapter trimming and quality control checks using Trim Galore version 0.6.5 (Cutadapt and FastQC). Throughout the computational analysis parallel processing was performed using GNU Parallel (7). Processed reads were aligned to the Arabidopsis thaliana genome (TAIR10) using the Rsubread align function (version 2.14.0). Low quality alignments (mapping quality < 2) and alignments to the mitochondrial and chloroplast genomes were removed using the Samtools view function (version 1.17). Alignments in a region of chromosome 2 (3239001 – 3510171) with abnormally high ATAC-seq signal in all samples were removed prior to further processing using BEDtools (version 2.30) (8). Reads derived from PCR duplicates were marked for exclusion using the Picard tools function Markduplicates (version 1.141). ATAC-seq peaks were called across all biological replicates using Genrich (9) with the following parameters: -r -d -j -p 0.01 -a 200. Peaks were then merged across all samples using the BEDtools merge function to generate a master list of peaks. ATAC-seq alignments were then assigned to peaks and counted using the Rsubread featureCounts function and the output from this function was used to calculate Fraction of Reads in Peaks scores (FRiPs) for each library. Differential chromatin accessibility analysis was performed using DESeq2 (version 1.26.0). Regions were defined as significantly differentially accessible using the following thresholds: P adjusted value < 0.001 and fold change > 1.5 or 2 as indicated in associated figure legends. To visualize data using the Integrated Genome Browser (IGV), bigwig coverage tracks were generated on merged replicate bam files using the deepTools (version 3.5.0) bamCoverage function (bin size of 1 bp and normalization by RPKM). Homer software (version 2.1.2) (10) was used to annotate ACRs and to assign ACRs to the nearest downstream transcript (within -2.5 kb and +0.5 kb). Gene ontology (GO) term enrichment analyses were performed with the Panther system, and by applying a binomial test with p-values adjusted for multiple testing by a Bonferroni correction. Heatmaps and metaplots were generated with DeepTools. Homer software was used for de novo motif discovery among differentially accessible ACRs and to match discovered motifs to previously known motifs from published databases. We used ChIPpeakAnno software (Version 3.24) (11) to assign ACRs to annotated genomic features and to test for genomic overlap among different sets of peaks.

DAP-seq Analysis

To control for differences in data analysis between studies, previously published DAP-seq datasets GSE60143 (12) and PRJNA682697 (13) were reanalyzed. Raw FASTQ files were downloaded from SRA and processed to remove adapters using Trim Galore. Reads were aligned to the *Arabidopsis thaliana* genome using the Rsubread *align* function and low-quality alignments (mapping quality < 2) were removed using the Samtools *view* function. DAP-seq peaks were called using the MACS2 *callpeak* function with the following parameters: –keep-dup 1 --gsize 1.2e8 (version 2.2.7). For ABF1/2/3/4 DAP-seq datasets, peaks were merged across four replicate experiments. Bigwig files were generated on merged DAP-seq bam files using the deepTools (version 3.5.0) *bamCoverage* function (bin size of 1 bp and normalized via RPKM). DeepTools software was used to generate heatmaps and Metaprofile plots centered over ABA-regulated ACRs.

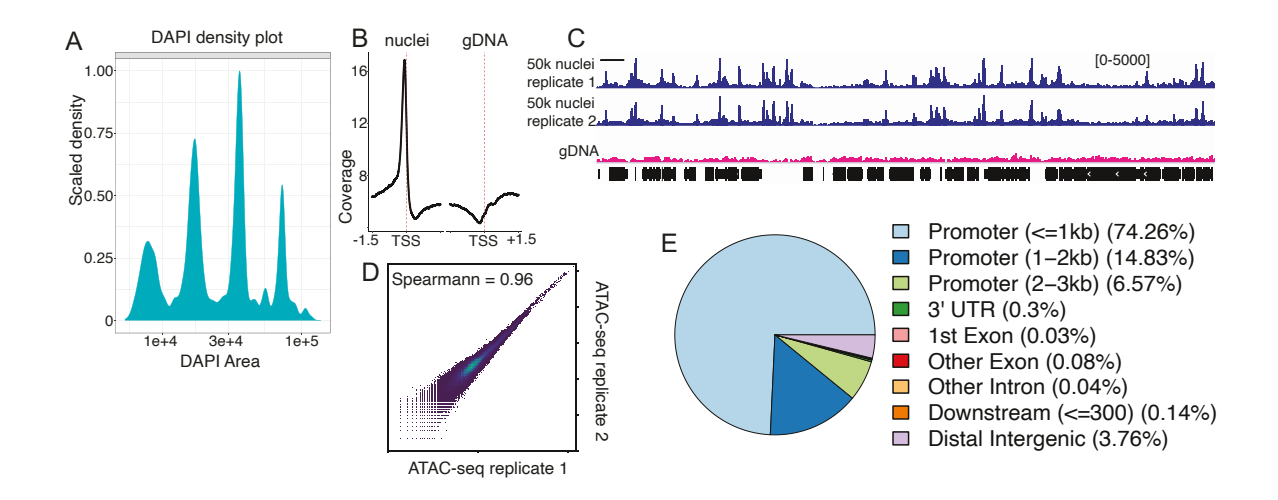


Fig. S1. FANS-ATAC-seq on seedling nuclei reproducibly measures chromatin accessibility in regulatory DNA. A) Density plot of DAPI fluorescence shows the distribution of ploidy among FACS-sorted nuclei from seedlings. B) Open chromatin reads (<100 bp) from a seedling ATAC-seq library show strong enrichment upstream of transcription start sites (TSS) (on left), while reads originating from an ATAC-seq library derived from purified *Arabidopsis* genomic DNA (gDNA) show no such enrichment (on right). C) Genome browser snapshot of a region of chromosome 1 showing ATAC-seq signal derived from either 50,000 seedling nuclei (two replicates shown in blue) or from purified genomic DNA (in pink). D) Scatterplot of ATAC-seq coverage showing correlation between two ATAC-seq replicates. E) Genomic distribution of seedling nuclei ATAC-seq peaks among annotated features.

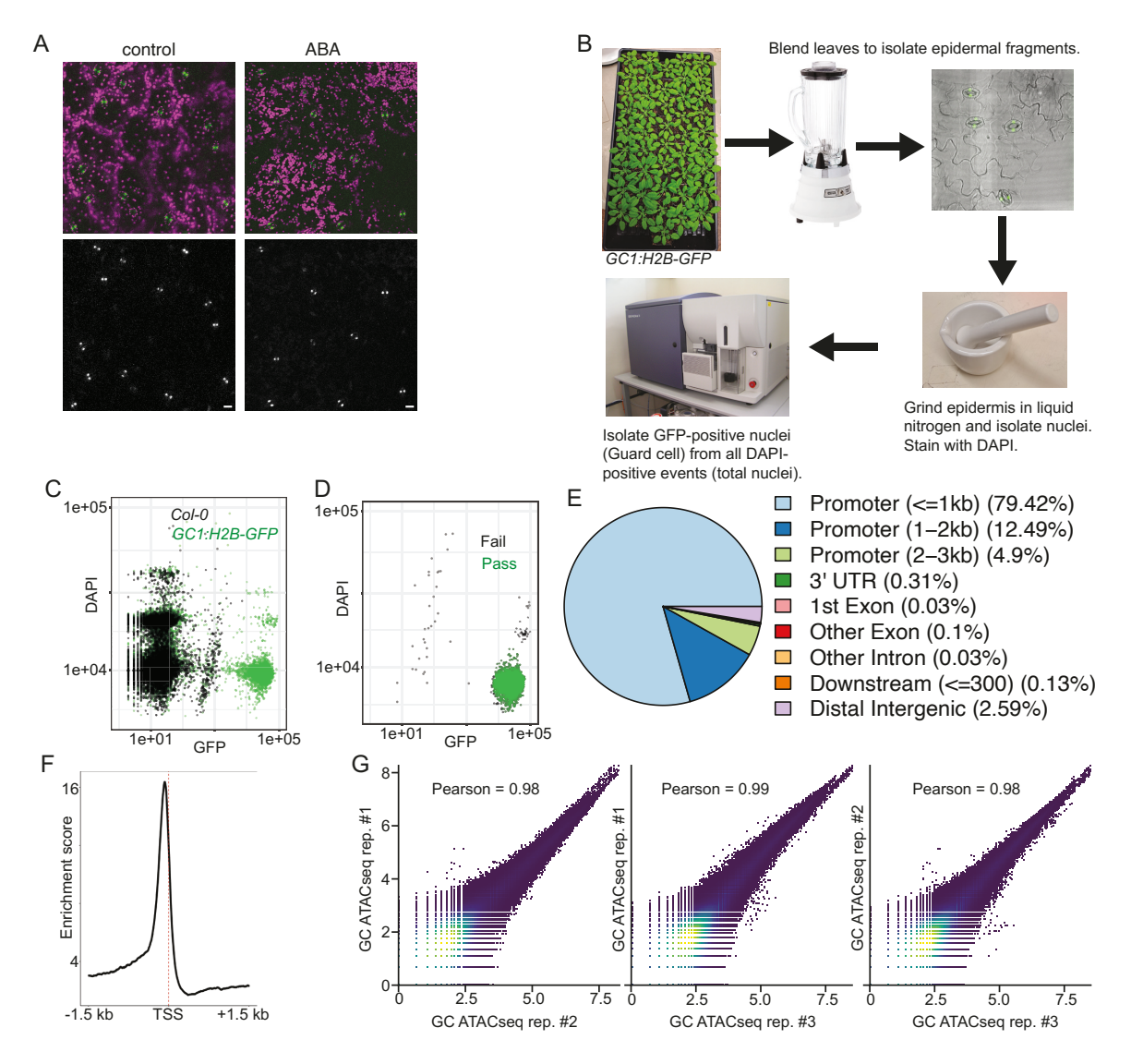


Fig. S2. Guard cell FANS-ATAC-seq. A) Micrographs from confocal imaging of 5-week-old pGC1:H2B-GFP leaves treated with either control or ABA for 4 hr. Images on top show merged GFP (green) and chlorophyll fluorescence (magenta). Bottom images show GFP signal only. B) Diagram of the protocol used to isolate guard cell nuclei from Arabidopsis plants. The leaves of roughly 40 6-week-old pGC1:H2b-GFP plants were blended in ice cold water. The resulting blendate was filtered through a 100 µm mesh sheet to isolate epidermal tissue. A representative fluorescence micrograph shows intact guard cells with nuclei labeled by H2b-GFP. Epidermal tissue was flash frozen in LN2 and then ground to a fine powder using a mortar and pestle. After extracting nuclei from ground tissue, GFP positive nuclei were purified using FACS. C) DAPI vs GFP intensity plot resulting from FACS analysis of nuclei from either pGC1:H2b-GFP plants (in green) or Col-0 plants (in black). D) Sorted guard cell nuclei were re-run through the same FACS protocol to evaluate the purity of the isolated population. The DAPI vs GFP plot shows nuclei passing (green) and failing (black) the sorting criteria. Out of 10,000 sorted nuclei, 9821 passed (purity of 98%). E) Pie chart displaying the distribution of guard cell ATAC-seq peaks among annotated genomic features. F) TSS enrichment plot of open chromatin reads (<100 bp) from a Guard Cell ATAC-seg library shows strong enrichment upstream of transcription start sites (TSSs). G) Scatterplots showing the correlation among biological replicates of guard cell ATACseg libraries.

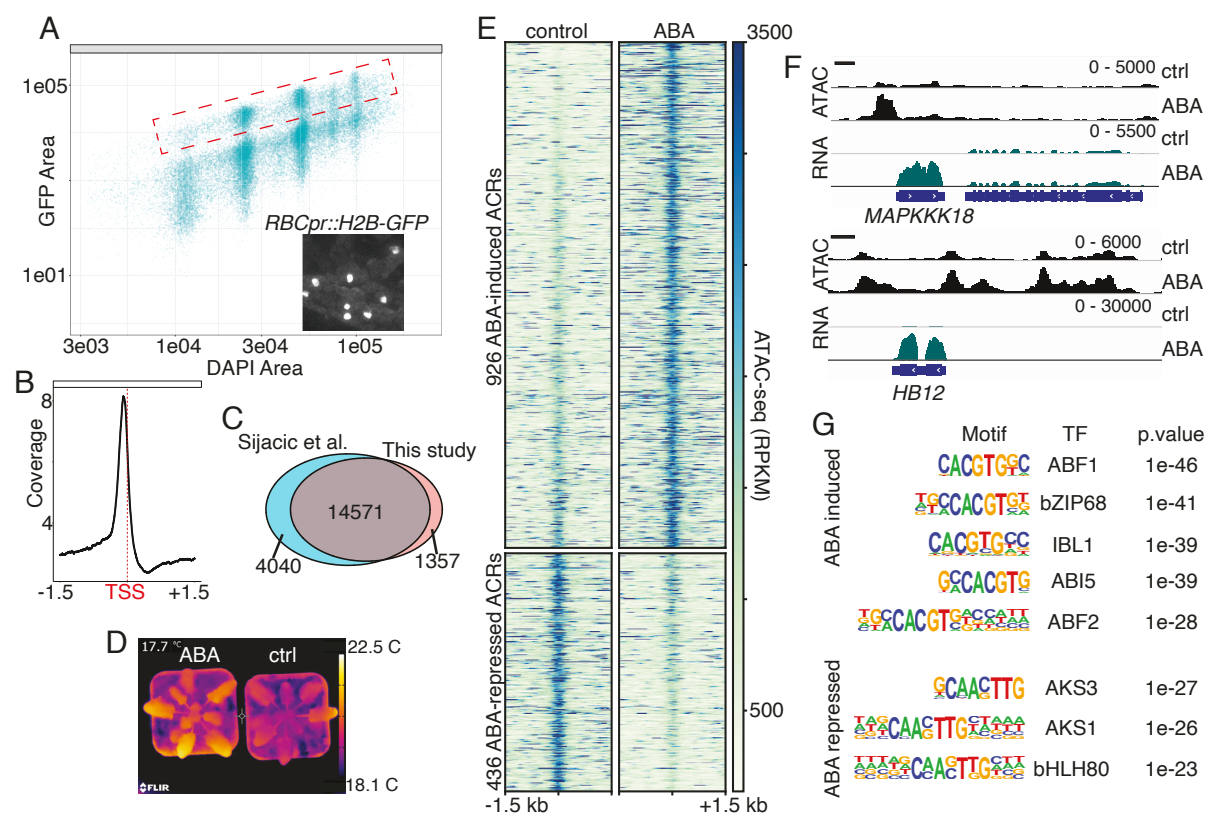


Fig. S3. ABA induced chromatin remodeling in mesophyll cell nuclei. **A)** GFP vs DAPI intensity plot showing the results of FACS analysis on nuclei from *RBCpr::H2b-GFP* plants. The location of GFP positive mesophyll nuclei sorted for ATAC-seq is indicated by a red dashed box. Inset shows a confocal image showing the expression of *RBCpr::H2b-GFP* in mesophyll cell nuclei. **B)** ATAC-seq coverage plot showing strong enrichment of mesophyll ATAC-seq reads upstream of Transcription Start Sites (TSSs). **C)** Overlap of mesophyll ATAC-seq peaks from (14) with those from this study. **D)** Representative infrared image showing increase in leaf surface temperature 3hrs after spraying *RBCpr:H2b-GFP* plants with ABA. **E)** Heatmap of ATAC-seq signal in mesophyll nuclei at regions showing ABA-regulated chromatin accessibility. ABA significantly increased accessibility at 926 regions and decreased accessibility at 436 regions (FDR < 0.001 and FC > 1.5). **F)** Genome browser snapshots at representative genes (*MAPKKK18* and HB12) showing ABA-regulated chromatin accessibility in upstream sequences. **G)** Selection of transcription factor binding motifs enriched in ABA-induced and ABA-repressed ATAC-seq regions in mesophyll nuclei.

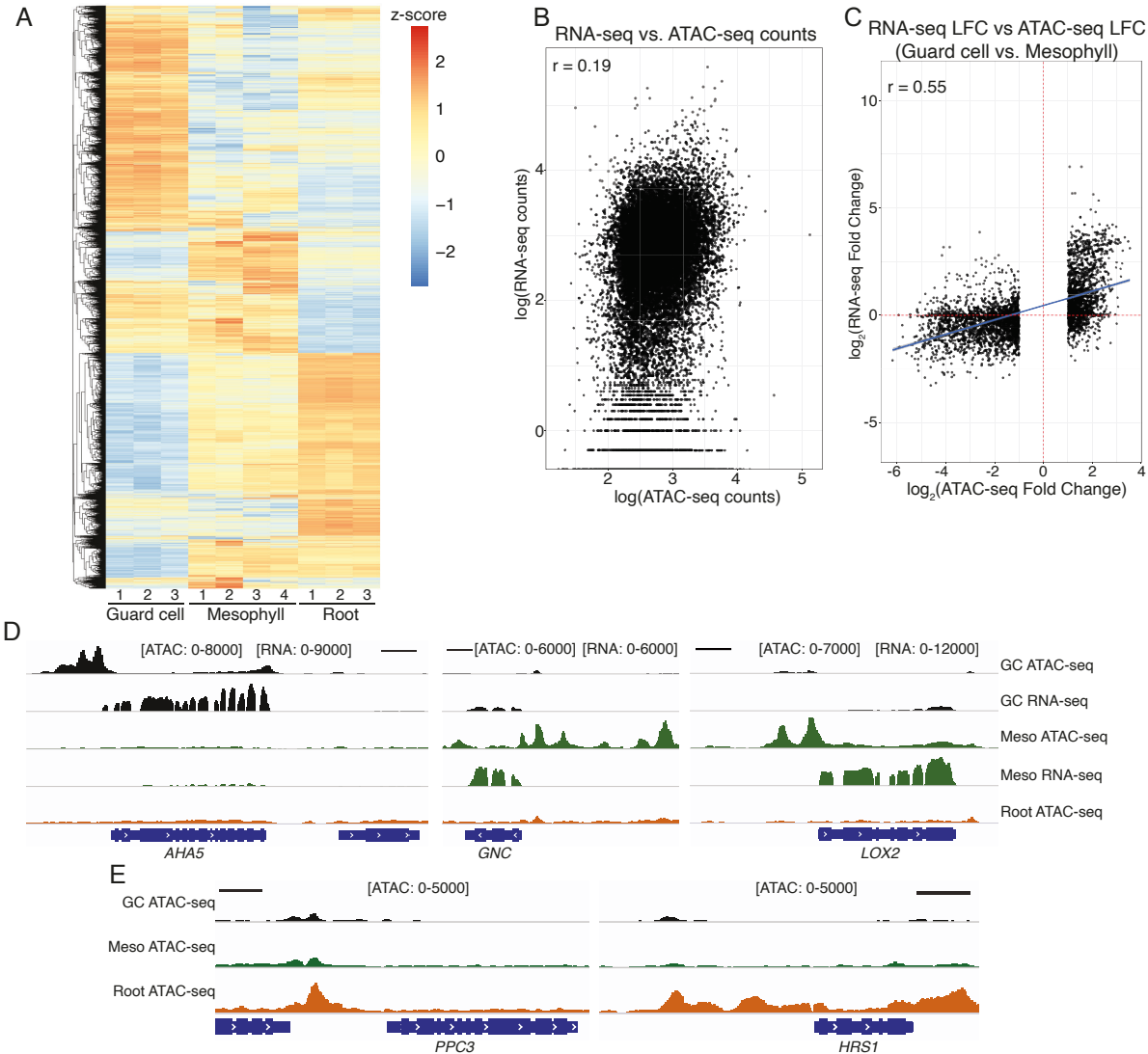


Fig. S4. Patterns of chromatin accessibility in guard cells, mesophyll cells, and roots. A) Clustered heat map of normalized ATAC-seq signal plotted over all ACRs identified across samples (30,985 peaks). The indicated samples are split by biological replicate, and ATAC-seq signal is normalized by z-score across rows. B) Scatterplot of upstream chromatin accessibility (ACRs between -2.5 kb and +0.5 kb of a transcription start site) and downstream gene transcript levels. ATAC-seg and RNA-seg values are plotted as log(counts). The Pearson's correlation coefficient derived from this comparison is indicated on the plot. C) Scatter plot showing the relationship between fold-change in ATAC-seg signal at cell-type regulated ACRs (Guard Cell vs. Mesophyll) and fold-changes in downstream transcript levels. ACRs residing within -2.5 kb and +0.5 kb of a transcription start site were assigned to nearest gene. A linear trend line (blue) with 95% confidence interval (in gray) is shown. The Pearson's correlation coefficient derived from this comparison is indicated on the plot. D) IGV browser displays of the indicated ATAC-seq and RNA-seq data highlighting examples of cell-type specific accessible chromatin, scale bars represent 1 kilobase. Guard cell specific open chromatin upstream of the plasma membrane H+-ATPase gene AHA5. Mesophyll-specific open chromatin upstream of the GATA transcription factor gene GNC. Mesophyll-specific open chromatin upstream of the lipoxygenase gene LOX2. E) IGV browser displays of the indicated ATAC-seg data highlighting examples of root specific open chromatin upstream of the phosphoenolpyruvate carboxylase gene PPC3 and upstream of the GARP-family transcription factor gene HRS1. Scale bars indicate 1 kilobase.

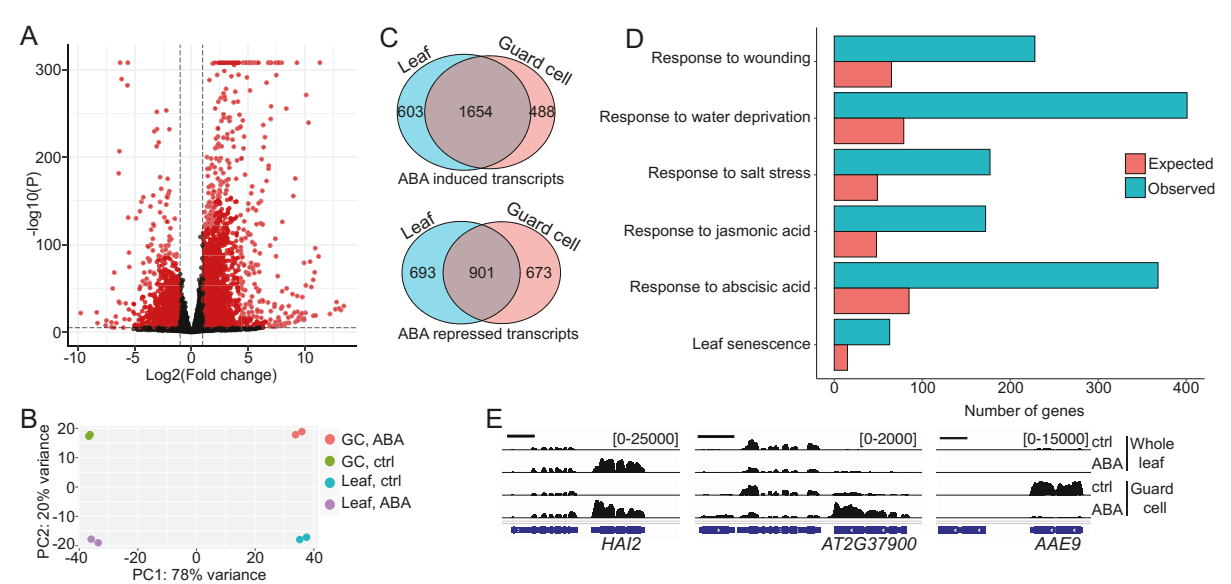


Fig. S5. RNA-seq identifies ABA-regulated transcripts in guard cells and whole leaf tissue. A) Volcano plot of differential whole leaf RNA-seq analysis (FDR < 0.001, FC > 2) comparing control and ABA-treated samples. Differentially expressed transcripts are colored in red (2257 upregulated and 1594 downregulated). **B)** Principal component analysis (PCA) of RNA-seq results showing samples clustering by treatment (ABA vs control) and cell-type (guard cell vs leaf). **C)** Overlap of transcripts induced or repressed by ABA between whole leaves and guard cells. **D)** Results of a Gene Ontology (GO) enrichment analysis performed on ABA-induced transcripts in guard cells. The bar plot shows the number of ABA-induced genes observed in each enriched GO category vs the number of genes expected by chance. **E)** Genome browser snapshots showing RNA-seq signal from the indicated samples at the representative ABA-regulated genes *HAI2*, *AT2G37900*, and *AAE9*.

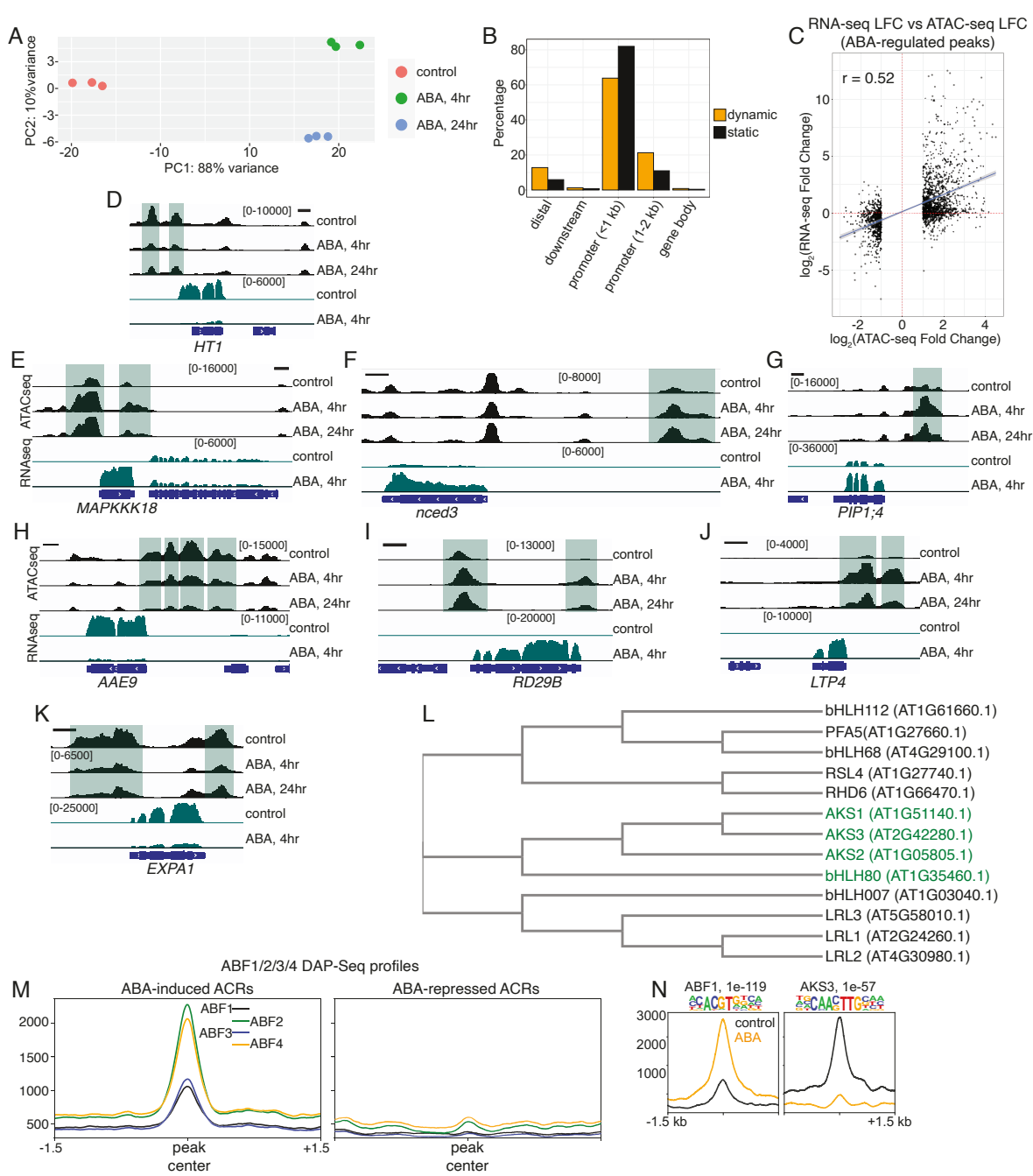


Fig. S6. ABA triggered chromatin remodeling in guard cells. A) PCA plot of guard cell ATAC-seq samples from ABA treatment experiments. B) Genomic distribution among annotated features of guard cell ATAC-seq peaks separated into regions that are static (black) and those that are ABA-regulated (orange). C) Scatter plot showing the relationship between fold-change in ATAC-seq signal at ABA-regulated ACRs in guard cells and fold-change in downstream transcript levels in guard cells. ACRs residing within -2.5 kb and +0.5 kb of a transcription start site were assigned to nearest gene. A linear trend line (blue) with 95% confidence interval (in gray) is shown. The Pearson's correlation coefficient derived from this comparison is indicated on the plot. D-K) IGV images (scale bars indicate 1 kb and grey-green shading indicates approximate position of differentially accessible regions) showing additional examples of ABA-induced changes to chromatin accessibility upstream of D) HT1 which encodes a kinase controlling low CO₂ induced stomatal opening, E) the ABA-activated kinase MAPKKK18, F) ABA biosynthesis gene NCED3, G) the aquaporin PIP1;4, H) the wax biosynthesis gene AAE9, I) RD29B, J) LTP4,

and **K)** the cell wall expansin gene *EXPA1*. **L)** Cladogram generated from multiple sequence alignment (ClustalW) of related *Arabidopsis* bHLH transcription factors. TFs with motifs enriched in ABA-repressed ACRs are highlighted in green. **M)** Metaprofile plots of DAP-seq signal (RPKM-normalized) for ABF1/2/3/4 centered over ABA-induced or ABA-repressed ACRs. **N)** De novo motif discovery uncovered motifs similar to ABF1 and AKS3 in ABA-activated and ABA-repressed ACRs, respectively. The p-value associated with this enrichment is shown. Below the uncovered motifs are metaplots of ATAC-seq signal (RPKM-normalized) from either control or ABA-treated guard cells centered over peaks containing these motifs.

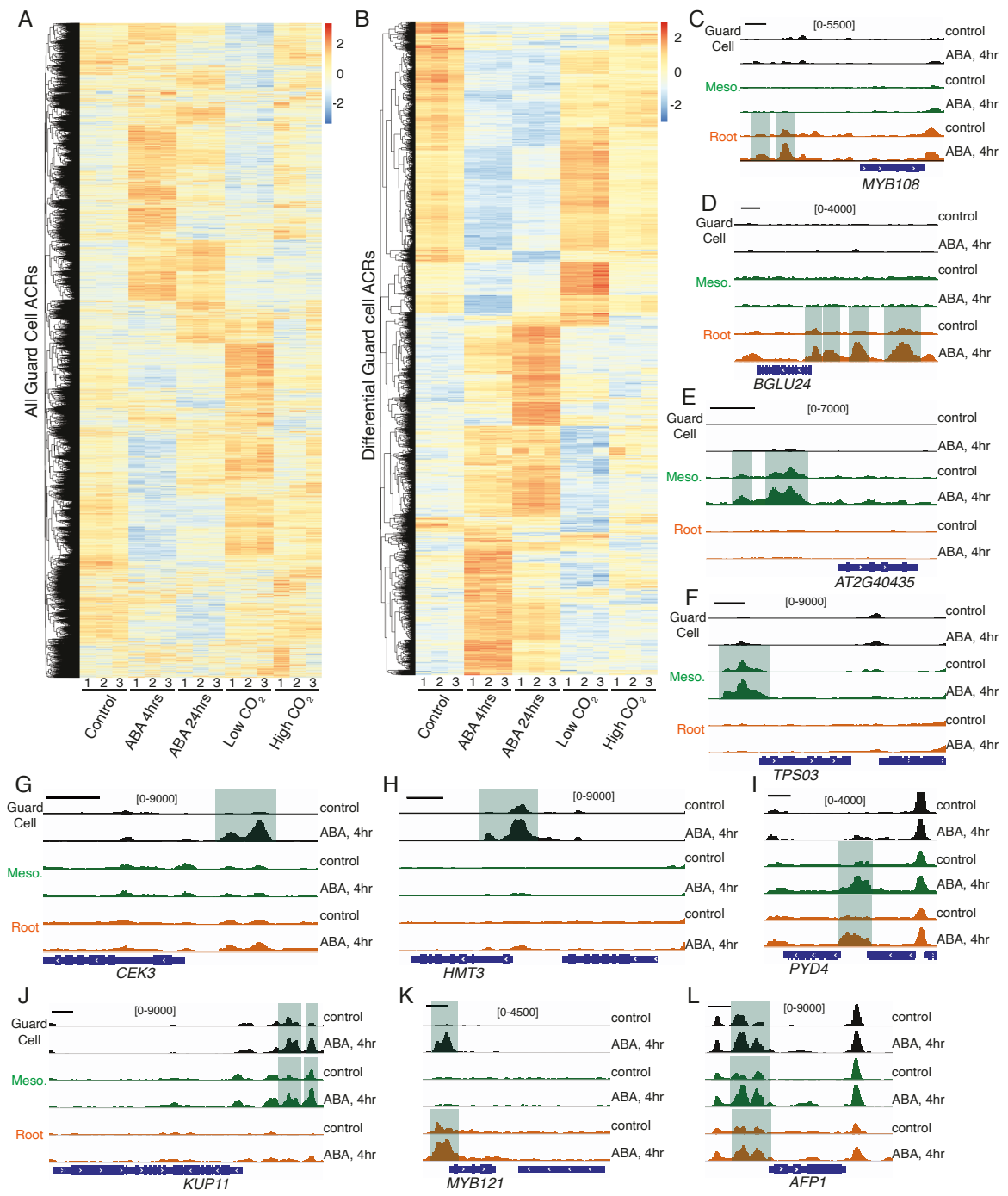


Fig. S7. Chromatin dynamics in guard cells and examples of cell-type specificity. A) Clustered heat map of normalized ATAC-seq signal plotted over all ACRs (22680 peaks) identified in guard cells. The indicated samples are split by biological replicate, and ATAC-seq signal is normalized by z-score across rows. B) Clustered heat map of normalized guard cell ATAC-seq signal plotted over differential ACRs across all treatments (4473 peaks). The indicated samples are split by biological replicate, and ATAC-seq signal is normalized by z-score across rows. C-L) Genome browser images showing examples of cell/tissue-type specific ABA chromatin dynamics. Scale bars represent 1 kilobase and the relative positions of differential ACRs are indicated by green highlighting. Root specific changes to chromatin accessibility upstream of C) the MYB transcription factor gene *MYB108* and D) the beta glucosidase gene *BGLU24*. Mesophyll-specific ABA-induced chromatin dynamics upstream of E) the SCREAM-like gene

AT2G40435 and **F**) the terpene synthase gene *TPS03*. Guard cell specific ABA-induced chromatin dynamics upstream of **G**) the choline synthase gene *CEK3* and **H**) the homocysteine S-methyltransferase gene *HMT3*. Examples of ABA-induced chromatin dynamics common to multiple cell/tissue-types upstream of **I**) the gene *PYD4*, **J**) the potassium transporter gene *KUP11*, **K**) the MYB-transcription factor gene *MYB121*, and **L**) the ABI5 binding protein gene *AFP1*.

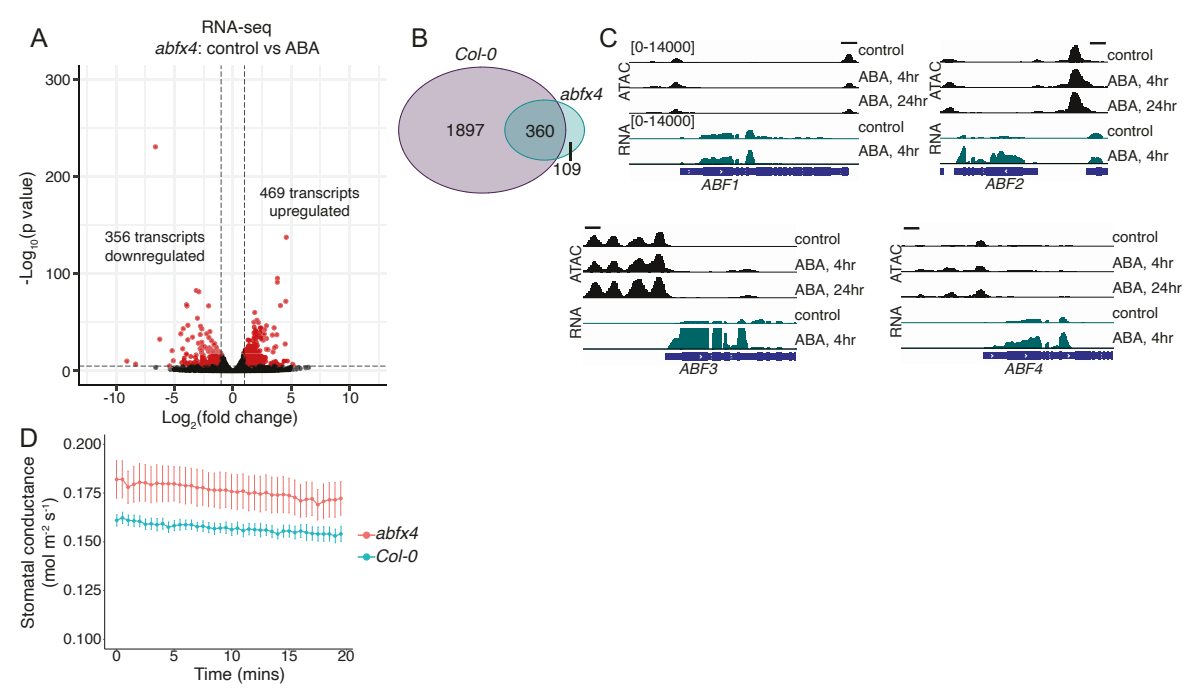


Fig S8. The ABRE binding proteins ABF1/2/3/4 are required for the bulk of ABA-induced transcription in mature leaf tissue. A) Volcano plot of RNA-seq results from ABA or control treated 5-week-old abfx4 mutant leaf tissue. ABA significantly upregulated 469 transcripts and downregulated 356 transcripts (FDR < 0.001 and FC > 2). B) Overlap of ABA-induced transcripts in Col-0 leaves vs abfx4 mutant leaves shows that ABFs are required for the upregulation of 2030 transcripts. C) Genome browser snapshots showing guard cell ATAC-seq signal and RNA-seq signal at four genes encoding ABF proteins. Chromatin accessibility upstream of ABF1-4 was not significantly increased by ABA in guard cells. D) Gas exchange analysis (Licor-6400) comparing steady state stomatal conductance of well-watered Col-0 and abf1/2/3/4 plants (n = 5 per genotype).

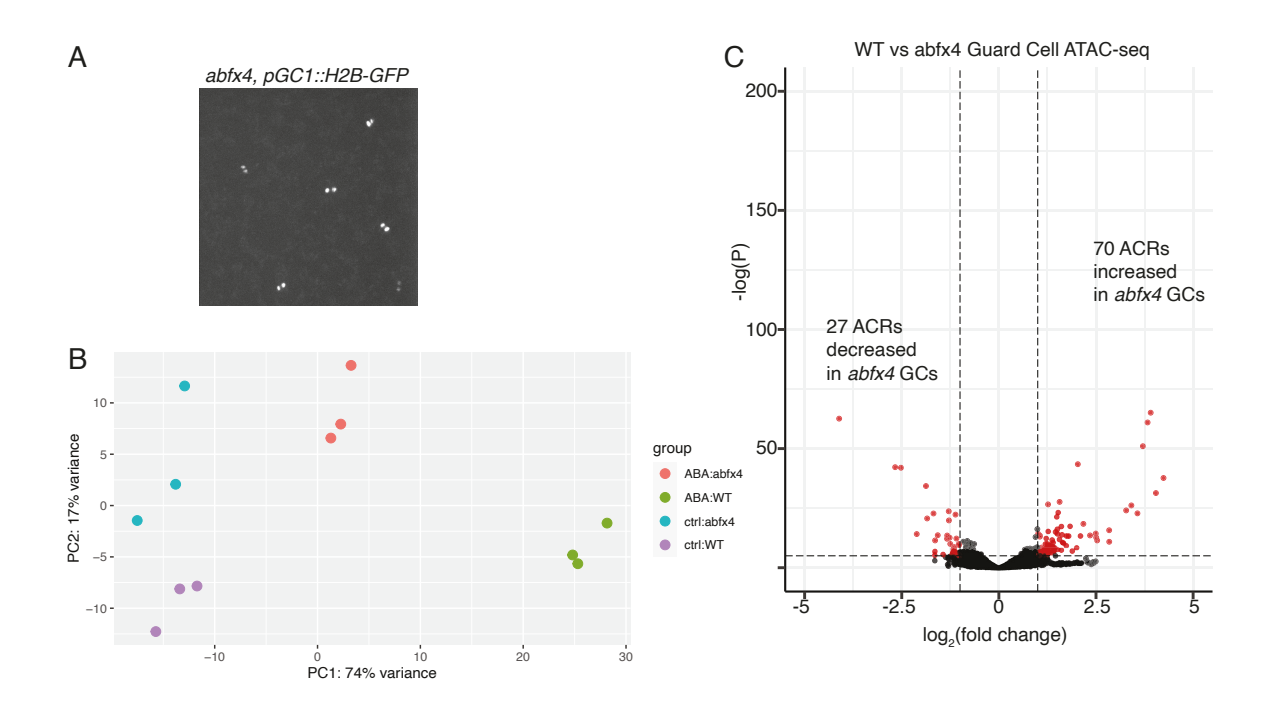


Fig S9. Chromatin accessibility in *abfx4* mutant guard cells without ABA treatment. A) Confocal image showing guard cell specific expression of H2B-GFP in *abfx4* mutant leaf. B) Principal component analysis (PCA) of Guard cell ATAC-seq results showing samples clustering by treatment (ABA vs control) and genotype (Col-0 vs abfx4). C) Volcano plot summarizing differential ATAC-seq analysis (FDR < 0.001 and FC > 2.0) comparing chromatin accessibility in control treated WT vs abfx4 mutant guard cells. Significantly differentially accessible peaks are colored in red.

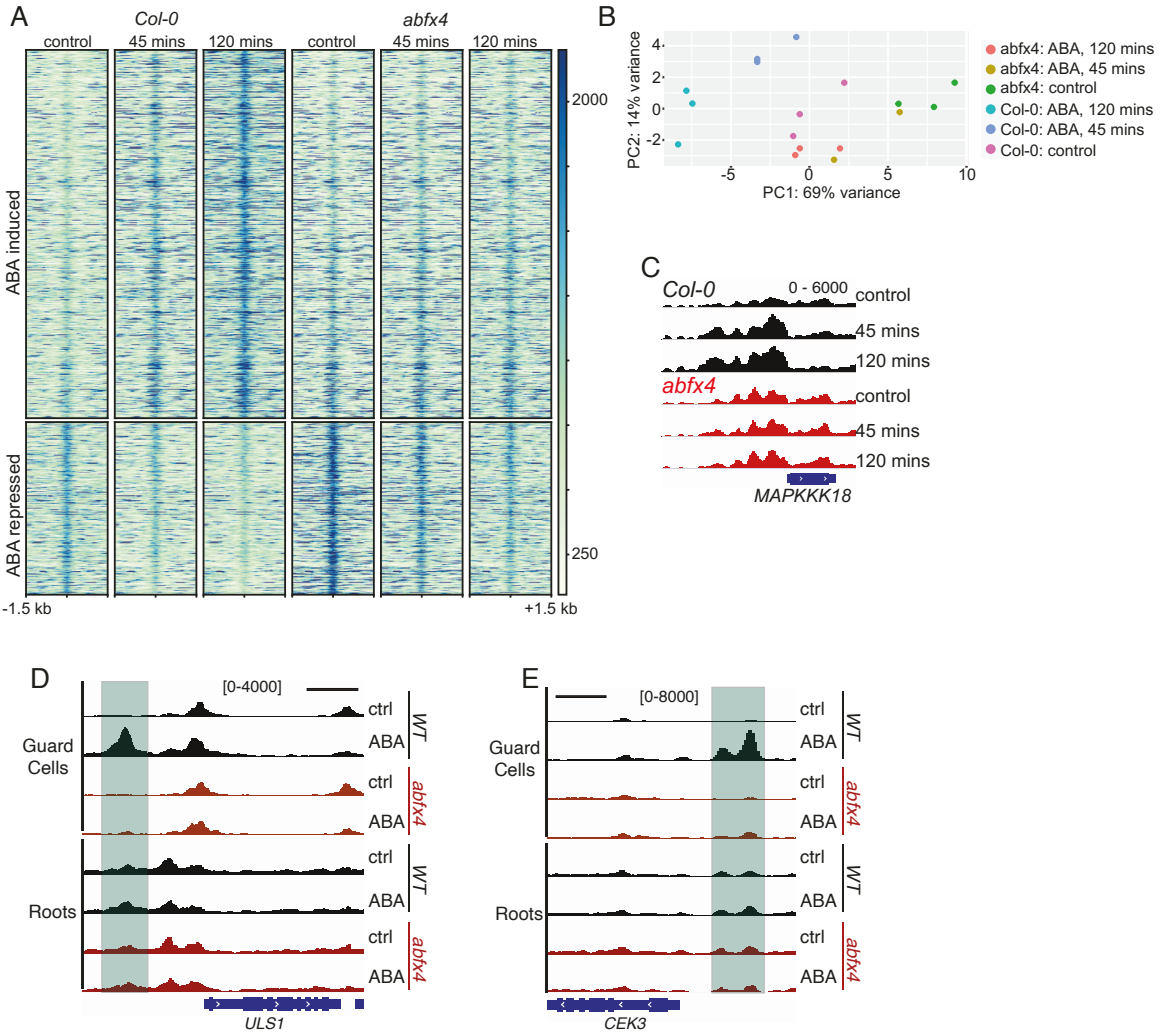


Fig S10. ABFs are required for ABA-induced chromatin opening in roots. A) Heatmap of ATAC-seq signal (RPKM-normalized) at regions showing ABA-regulated chromatin accessibility over the indicated ABA treatment time course in either *WT* or *abfx4* mutant root nuclei. **B)** Principal component analysis of root ATAC-seq libraries showing separation of samples by both genotype and ABA treatment duration. **C)** Genome browser snapshot showing chromatin accessibility in *WT* or *abfx4* mutant root nuclei upstream of the ABA-induced gene *MAPKKK18* over the indicated ABA treatment time series. **D, E)** Genome browser snapshots showing guard cell specific and ABF-dependent ABA-induced ACRs upstream of the genes *CEK1* and *ULS1*. Scale bars indicate 1 kb.

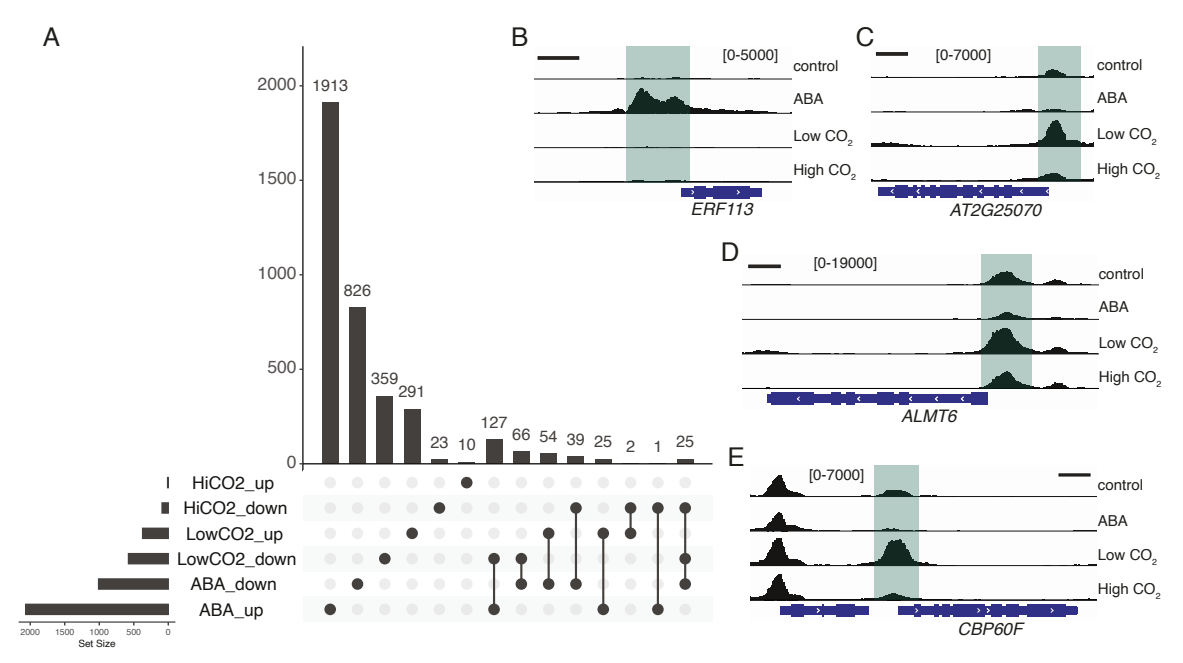


Fig S11. Distinct regulation of chromatin by ABA and CO₂ in guard cells. A) UpSet plot showing the set relationships between ABA, low CO₂, and high CO₂ regulated ATAC-seq peaks. The y-axis of the bar-plot shows the number of peaks found in the set intersections indicated along the x-axis. The sets being comparing are indicated by lines connecting filled in circles. **B-E)** Genome browser images (scale bars indicate 1 kb) of ATAC-seq signal (RPKM-normalized) showing ABA and CO₂-regulated chromatin accessibility upstream of **B)** *ERF113*, **C)** *AT2G25070*, **D)** *ALMT6*, and **E)** *CBP60F*.

Supplementary Datasets

Dataset S1. Summary of sequencing libraries. Excel file containing 1 sheet.

Dataset S2. Annotated lists of all ATAC-seq peaks called in different cell/tissue-types. Annotations include genomic coordinates, distance to nearest transcription start site, and nearest gene name and description. Excel file containing 10 sheets:

- 1) Annotated list of all ACRs called in root nuclei ATAC-seq libraries.
- 2) Annotated lists of all ACRs called in Guard Cell nuclei ATAC-seq libraries.
- 3) Annotated list of all ACRs called in Mesophyll cell nuclei ATAC-seg libraries.
- 4) Annotated list of all ACRs called in Mesophyll cell ATAC-seg libraries from (14).
- 5) Annotated list of ACRs enriched in Root nuclei.
- 6) Annotated list of ACRs enriched in Mesophyll cell nuclei.
- 7) Annotated list of ACRs enriched in Guard Cell nuclei.
- 8) Master list of merged ATAC-seq peaks from called across all tissues/cell-types.
- **9)** Master list of merged ATAC-seq peaks called in root ATAC-seq samples across all treatments and genotypes.
- **10)** Master list of merged ATAC-seq peaks called in guard cell ATAC-seq samples across all treatments and genotypes.

Dataset S3. Annotated lists of all differentially accessible ACRs. Annotations include genomic coordinates, distance to nearest transcription start site, and nearest gene name and description. Datasets also contain results of differential chromatin accessibility analysis including log2(Foldchange) and adjusted p-values. Excel file containing 13 sheets:

- 1) Annotated differentially accessible ACRs in whole seedings (control vs. 4 hours ABA).
- 2) Annotated differentially accessible ACRs in roots (control vs. 45 minutes ABA).
- 3) Annotated differentially accessible ACRs in roots (control vs 2 hours ABA).
- 4) Annotated differentially accessible ACRs in roots (control vs 4 hours ABA).
- **5)** Annotated differentially accessible ACRs in mesophyll nuclei (control vs 4 hours after ABA treatment).
- **6)** Annotated differentially accessible ACRs in guard cell nuclei (control vs 4 hours after ABA treatment).
- **7)** Annotated differentially accessible ACRs in guard cell nuclei (control vs 24 hours after ABA treatment).
- **8)** Annotated differentially accessible ACRs in guard cell nuclei (no treatment, WT vs. *abfx4* mutant).
- **9)** Annotated differentially accessible ACRs in *abfx4* mutant guard cell nuclei (control vs. 4 hours after ABA treatment).
- **10)** Annotated differentially accessible ACRs in *abfx4* mutant root nuclei (control vs. 45 minutes ABA).
- 11) Annotated differentially accessible ACRs in abfx4 mutant root nuclei (control vs 2 hours ABA).
- 12) Annotated differentially accessible ACRs in guard cell nuclei (control vs. 100 ppm CO₂).
- 13) Annotated differentially accessible ACRs in guard cell nuclei (control vs 1000 ppm CO₂).

Dataset S4. Table containing annotated high confidence guard cell specific ACRs ranked by downstream gene transcript level in guard cells. Excel file containing 1 sheet.

Dataset S5. ABA-regulated transcripts in whole leaves and guard cells. Excel file containing 2 sheets:

- 1) Differentially expressed genes in whole leaves (control vs. 4 hours after ABA treatment).
- 2) Differentially expressed genes in guard cells (control vs 4 hours after ABA treatment).

Dataset S6. Table containing results of Gene Ontology (GO) term analyses of genes downstream of ABA-regulated ACRs. Excel file containing 6 sheets:

- 1) GO terms enriched among genes downstream of ABA (4 hr)-induced ACRs in roots.
- 2) GO terms enriched among genes downstream of ABA (4 hr)-repressed ACRs in roots.
- 3) GO terms enriched among genes downstream of ABA (4 hr)-induced ACRs in guard cells.
- 4) GO terms enriched among genes downstream of ABA (4hr)-repressed ACRs in guard cells.
- 5) GO terms enriched among genes downstream of ABA (24 hr)-induced ACRs in guard cells.
- 6) GO terms enriched among genes downstream of ABA (24 hr)-repressed ACRs in guard cells.

Dataset S7. Table containing Top 10 transcription factor binding motifs identified among different sets of differentially accessible ATAC-seq peaks.

Dataset S8. Table of primer sequences. Excel file containing 1 sheet.

SI References

- 1. Y. Liao, G. K. Smyth, W. Shi, The R package Rsubread is easier, faster, cheaper and better for alignment and quantification of RNA sequencing reads. *Nucleic Acids Research* **47**, e47 (2019).
- 2. H. Li, et al., The Sequence Alignment/Map format and SAMtools. *Bioinformatics* **25**, 2078–2079 (2009).

- 3. M. I. Love, W. Huber, S. Anders, Moderated estimation of fold change and dispersion for RNA-seg data with DESeq2. *Genome Biology* **15**, 550 (2014).
- 4. F. Ramírez, et al., deepTools2: a next generation web server for deep-sequencing data analysis. *Nucleic Acids Research* **44**, W160–W165 (2016).
- 5. H. Mi, A. Muruganujan, D. Ebert, X. Huang, P. D. Thomas, PANTHER version 14: more genomes, a new PANTHER GO-slim and improvements in enrichment analysis tools. *Nucleic Acids Research* **47**, D419–D426 (2019).
- 6. J. Buenrostro, B. Wu, H. Chang, W. Greenleaf, ATAC-seq: A Method for Assaying Chromatin Accessibility Genome-Wide. *Curr Protoc Mol Biol* **109**, 21.29.1-21.29.9 (2015).
- O. Tange, GNU Parallel 20220922 ('Elizabeth'). Zenodo (2022) https://doi.org/10.5281/zenodo.7105792.
- 8. A. R. Quinlan, I. M. Hall, BEDTools: a flexible suite of utilities for comparing genomic features. *Bioinformatics* **26**, 841–842 (2010).
- 9. J. M. Gaspar, Genrich: detecting sites of genomic enrichment (2021).
- S. Heinz, et al., Simple Combinations of Lineage-Determining Transcription Factors Prime cis-Regulatory Elements Required for Macrophage and B Cell Identities. Molecular Cell 38, 576–589 (2010).
- 11. L. J. Zhu, *et al.*, ChIPpeakAnno: a Bioconductor package to annotate ChIP-seq and ChIP-chip data. *BMC Bioinformatics* **11**, 237 (2010).
- 12. R. C. O'Malley, *et al.*, Cistrome and Epicistrome Features Shape the Regulatory DNA Landscape. *Cell* **165**, 1280–1292 (2016).
- 13. Y. Sun, et al., Divergence in the ABA gene regulatory network underlies differential growth control. *Nat. Plants*, 1–12 (2022).
- 14. P. Sijacic, M. Bajic, E. C. McKinney, R. B. Meagher, R. B. Deal, Changes in chromatin accessibility between Arabidopsis stem cells and mesophyll cells illuminate cell type-specific transcription factor networks. *The Plant Journal* **94**, 215–231 (2018).